The Astrophysical Journal, 830:126 (17pp), 2016 October 20 doi:10.3847/0004-637X/830/2/126


# THE CARINA PROJECT. X. ON THE KINEMATICS OF OLD AND INTERMEDIATE-AGE STELLAR POPULATIONS*†

M. Fabrizio[1,2], G. Bono[3,4], M. Nonino[5], E. L. Łokas[6], I. Ferraro[4], G. Iannicola[4], R. Buonanno[1,2], S. Cassisi[2], G. Coppola[7], M. Dall'Ora[7], R. Gilmozzi[8], M. Marconi[7], M. Monelli[9,10], M. Romaniello[8,11], P. B. Stetson[12], F. Thévenin[13], and A. R. Walker[14]

[1] ASI Science Data Center, Via del Politecnico s.n.c., I-00133 Rome, Italy; fabrizio@oa-teramo.inaf.it
[2] INAF-Osservatorio Astronomico di Teramo, Via Mentore Maggini s.n.c., I-64100 Teramo, Italy
[3] Dipartimento di Fisica, Università di Roma "Tor Vergata," Via della Ricerca Scientifica 1, I-00133 Roma, Italy
[4] INAF-Osservatorio Astronomico di Roma, Via Frascati 33, I-00040 Monte Porzio Catone (RM), Italy
[5] INAF-Osservatorio Astronomico di Trieste, Via G.B. Tiepolo 11, I-40131 Trieste, Italy
[6] Nicolaus Copernicus Astronomical Center, Bartycka 18, 00-716 Warsaw, Poland
[7] INAF-Osservatorio Astronomico di Capodimonte, Salita Moiariello 16, I-80131 Napoli, Italy
[8] European Southern Observatory, Karl-Schwarzschild-Str. 2, D-85748 Garching bei München, Germany
[9] Instituto de Astrofísica de Canarias, Calle Via Lactea s/n, E-38200 La Laguna, Tenerife, Spain
[10] Departamento de Astrofísica, Universidad de La Laguna, E-38200 La Laguna, Tenerife, Spain
[11] Excellence Cluster universe, Boltzmannstr. 2, D-85748, Garching bei München, Germany
[12] Dominion Astrophysical Observatory, NRC-Herzberg, National Research Council, 5071 West Saanich Road, Victoria, BC V9E 2E7, Canada
[13] Université de Nice Sophia-antipolis, CNRS, Observatoire de la Côte d'Azur, Laboratoire Lagrange, BP 4229, F-06304 Nice, France
[14] Cerro Tololo Inter-American Observatory, National Optical Astronomy Observatory, Casilla 603, La Serena, Chile
*Received 2016 May 20; revised 2016 July 11; accepted 2016 July 11; published 2016 October 17*

## ABSTRACT

We present new radial velocity (RV) measurements of old (horizontal branch) and intermediate-age (red clump) stellar tracers in the Carina dwarf spheroidal. They are based on more than 2200 low-resolution spectra collected with VIMOS at Very Large Telescope (VLT). The targets are faint ($20 \lesssim V \lesssim 21.5$ mag), but the accuracy at the faintest limit is $\leqslant 9$ km s$^{-1}$. These data were complemented with RV measurements either based on spectra collected with FORS2 and FLAMES/GIRAFFE at VLT or available in the literature. We ended up with a sample of 2748 stars and among them, 1389 are candidate Carina stars. We found that the intermediate-age stellar component shows a well-defined rotational pattern around the minor axis. The western and the eastern side of the galaxy differ by $+5$ and $-4$ km s$^{-1}$ when compared with the main RV peak. The old stellar component is characterized by a larger RV dispersion and does not show evidence of the RV pattern. We compared the observed RV distribution with *N*-body simulations for a former disky dwarf galaxy orbiting a giant Milky Way–like galaxy. We rotated the simulated galaxy by 60° with respect to the major axis, we kept the observer on the orbital plane of the dwarf and extracted a sample of stars similar to the observed one. Observed and predicted $V_{\rm rot}/\sigma$ ratios across the central regions are in remarkable agreement. This evidence indicates that Carina was a disky dwarf galaxy that experienced several strong tidal interactions with the Milky Way. Owing to these interactions, Carina transformed from a disky to a prolate spheroid and the rotational velocity transformed into random motions.

*Key words:* galaxies: dwarf – galaxies: individual (Carina) – galaxies: kinematics and dynamics – galaxies: stellar content

*Supporting material:* machine-readable table

## 1. INTRODUCTION

Dwarf galaxies are fundamental laboratories for cosmological, chemical evolution, synthetic stellar population, and evolutionary models. These systems have been the cross-road of paramount photometric and spectroscopic investigations aimed at constraining their star formation history, chemical evolution, and dark matter (DM) content. Multiband photometry based on either ground-based mosaic CCD cameras (Carney & Seitzer 1986; Mateo et al. 1991; Smecker-Hane et al. 1996; Majewski et al. 2000; Monelli et al. 2003; Tolstoy et al. 2009; Bono et al. 2010; Stetson et al. 2011) or space images (Monelli et al. 2010a, 2010b; Hidalgo et al. 2013; Skillman et al. 2014) provided the opportunity to identify the faint Turn-Off in several dwarf galaxies in the Local Volume and to perform robust separation of galaxy stars from both background galaxies and foreground stars using the color–color plane in several Local Group galaxies. The kinematic investigations typically lag when compared with the photometry.

However, during the last few years the use of multislit and multiobject spectrographs provided the opportunity to measure the radial velocity (RV) of stellar samples ranging from a few hundreds (WLM; Leaman et al. 2013) to a few thousands (Fornax, Walker & Peñarrubia 2011). These measurements are crucial to estimate the dynamical mass, and in turn to constrain the mass-to-light ratio of these intriguing systems. However, it is not clear yet whether dwarf irregulars are—at fixed total mass—less DM dominated than dwarf spheroidals (dSph; Woo et al. 2008; Sanna et al. 2010).

∗ During the preparation of this manuscript, Giuseppina Coppola passed away. Her ideas, dedication and personality will be greatly missed.

† Based on spectra either collected with VIMOS at ESO/VLT (090.D-0756 (B), P.I.: M. Fabrizio), or retrieved from the ESO/ST-ECF Science Archive Facility: FORS2 at ESO/VLT (072.D-0651(A), P.I.: G. Bono; 078.B-0567(A), P.I.: F. Thévenin); FLAMES/GIRAFFE-UVES at ESO/VLT (074.B-0415(A), 076.B-0146(A), P.I.: E. Tolstoy; 171.B-0520(A)(B)(C), 180.B-0806(B), P.I.: G. Gilmore); UVES at ESO/VLT (66.B-0320(A), P.I.: E. Tolstoy).

Recent findings also suggest that the well studied dSphs appear to have, within a factor of two, an universal mass profile (Mateo et al. 1993; Strigari et al. 2008; Walker et al. 2009b). Moreover, the increase in the sample size and in the RV precision provided the opportunity to identify kinematical substructures in several nearby dwarf galaxies. They have already been detected in Sextans (Walker et al. 2008), LeoI (Mateo et al. 2008), Fornax and Sculptor (Walker & Peñarrubia 2011), and Carina (Fabrizio et al. 2011).

The reason why we are interested in dSphs is threefold:

a. Empirical evidence indicates that dSphs and ultra-faint dwarfs are the smallest stellar systems to be DM dominated. Therefore, they can provide firm constraints on the smallest DM halos that can retain baryons.
b. Cosmological models suggest that dSphs are the fossil records of the Galactic halo. Therefore, their kinematic and chemical properties can provide firm constraints on the formation and evolution of the Milky Way.
c. Current cosmological models indicate that the density profile of DM halos is a steep power law toward the center (cusp-profile; Navarro et al. 1997). On the other hand, tentative empirical evidence indicates that several dSphs and Low-Surface-Brightness galaxies disclose a constant density profile (core profile; Kormendy & Freeman 2004). The key observable to settle this open problem is the rotation curve. The cusp model has a rotation curve that increases with the square root of the radius, whereas the core model has a rotation curve that increases linearly with radius (see also de Blok 2010). Carina is a perfect laboratory to address the formation and evolution of gas-poor dwarf galaxies.

This is the 10th paper of a series focused on the stellar populations of the Carina dSph. We have investigated the evolutionary and pulsation properties of stellar populations in Carina using homogeneous and accurate optical photometry, metallicity distributions, and kinematics. The structure of the paper is as follows. In Section 2 we present the different spectroscopic data sets adopted in the current investigation. Special attention was paid to data reduction and calibration of the new low-resolution VIMOS spectra and to the observing strategy (Section 2.1). The approach adopted to measure radial velocities and the analysis of the RV distributions is discussed in Section 3. Section 4 deals with the photometric index $c_{U,B,I}$ adopted to separate old and intermediate-age stellar populations along the Carina red giant branch (RGB). The RV maps of the Carina subpopulations are considered in Section 5, while the variation (radial and angular) of the velocity profiles is addressed in Section 6. In Section 7 we perform a detailed comparison between current RV distributions and recent $N$-body simulations provided by Łokas et al. (2015). Finally, Section 8 gives a summary of the current results together with a few remarks concerning the future of the Carina project.

## 2. SPECTROSCOPIC DATA SETS AND DATA REDUCTION

To constrain the Carina kinematical structure, we adopted data collected at four spectrographs mounted at the Very Large Telescope (VLT) of the European Southern Observatory (ESO). The spectral resolution of data ranges from 600 to 40,000, allowing us to obtain accurate RVs up to the horizontal branch (HB) magnitude level ($V \sim 21.5$ mag). The overlap between different data sets allowed us to provide solid constraints on possible systematic errors. The adopted data sets and the sample of Carina stars observed are the following:

*High Resolution.* The high spectral resolution sample includes 79 spectra for 64 stars collected with the Ultraviolet and Visual Echelle Spectrographs (UVES, $R \sim 40{,}000$; Dekker et al. 2000) either in fiber (FLAMES/UVES) or in slit (UVES) mode. This data set also includes 1983 spectra for 97 stars collected with three high-resolution grisms (HR10, HR13, HR14A) of the Fibre Large Array Multi Element Spectrograph multifiber spectrograph FLAMES/GIRAFFE (GHR, $R \sim 20{,}000$; Pasquini et al. 2002). As a whole, this data set mainly includes RG stars that are brighter than $V \sim 19.5$ mag. The typical accuracy of the RV measurements based on these spectra is better than 0.8 km s$^{-1}$ for the entire sample (Fabrizio et al. 2011, 2012b). The color–magnitude diagram (CMD) and the sky distribution of HR targets are shown in the top panels of Figure 1.

*Medium Resolution.* This data set includes more than $1.6 \times 10^4$ spectra for 1768 stars collected with the FLAMES/GIRAFFE multifiber spectrograph (GMR, $R \sim 6500$) using the grating LR08 centered on the NIR calcium triplet (middle panels of Figure 1). These spectra were complemented with 772 low-resolution ($R \sim 2500$, grisms: 1028z, 1400V) spectra for 324 stars collected with the multislit FOcal Reducer/low dispersion Spectrograph 2 (FORS2; Appenzeller et al. 1998). The typical accuracy of the RV measurements based on these spectra is better than 6–10 km s$^{-1}$ for the entire sample (Fabrizio et al. 2011). The key advantage of the current spectroscopic sample is that it covers the entire body of the galaxy, as well asvthe regions across the tidal radius ($r_t = 28\farcm8 \pm 3\farcm6$, Mateo 1998) and beyond ($\sim 0\fdg7$). Moreover and even more important, this sample covers a broad range in magnitudes ($17.5 \lesssim V \lesssim 23$ mag), which means a good overlap with HR spectra (60 objects) and the opportunity to trace different stellar populations: old, low-mass, helium burning stars ($t \sim 12$ Gyr, Horizontal Branch stars); intermediate-age, helium burning stars ($t \sim 6$ Gyr, Red Clump (RC) stars); and red giants (RG) that are a mix of old and intermediate-age stars (see the middle panels of Figure 1).

Note that both HR and MR spectra were discussed by Fabrizio et al. (2011) and Fabrizio et al. (2012b) to constrain the kinematical properties of the Carina dSph. The reader interested in a more detailed discussion concerning the data reduction and the calibration of the different instruments is referred to the quoted papers.

*Literature.* We collected RV measurements for 1506 stars provided by Walker et al. (2007) using the high-resolution (20,000–25,000) spectra collected with Michigan/MIKE fiber system (MMFS) at *Magellan* (see the bottom panels of Figure 1). The 909 objects in common allowed us to estimate possible systematics and we found that they are quite similar, with a difference of $\approx 0.7$ km s$^{-1}$ and a standard deviation of 11 km s$^{-1}$.

*Low Resolution.* This data set includes 2454 spectra for 332 stars collected with the multislit VIsible MultiObject Spectrograph (VIMOS, $R \sim 600$; Le Fèvre et al. 2003) using the MR-GG475 grism ($4800 \leqslant \lambda \leqslant 10{,}000$ Å) during 2012 December and 2013 January.[15] This is a new data set and is

[15] 090.D-0756(B), P.I.: M. Fabrizio.

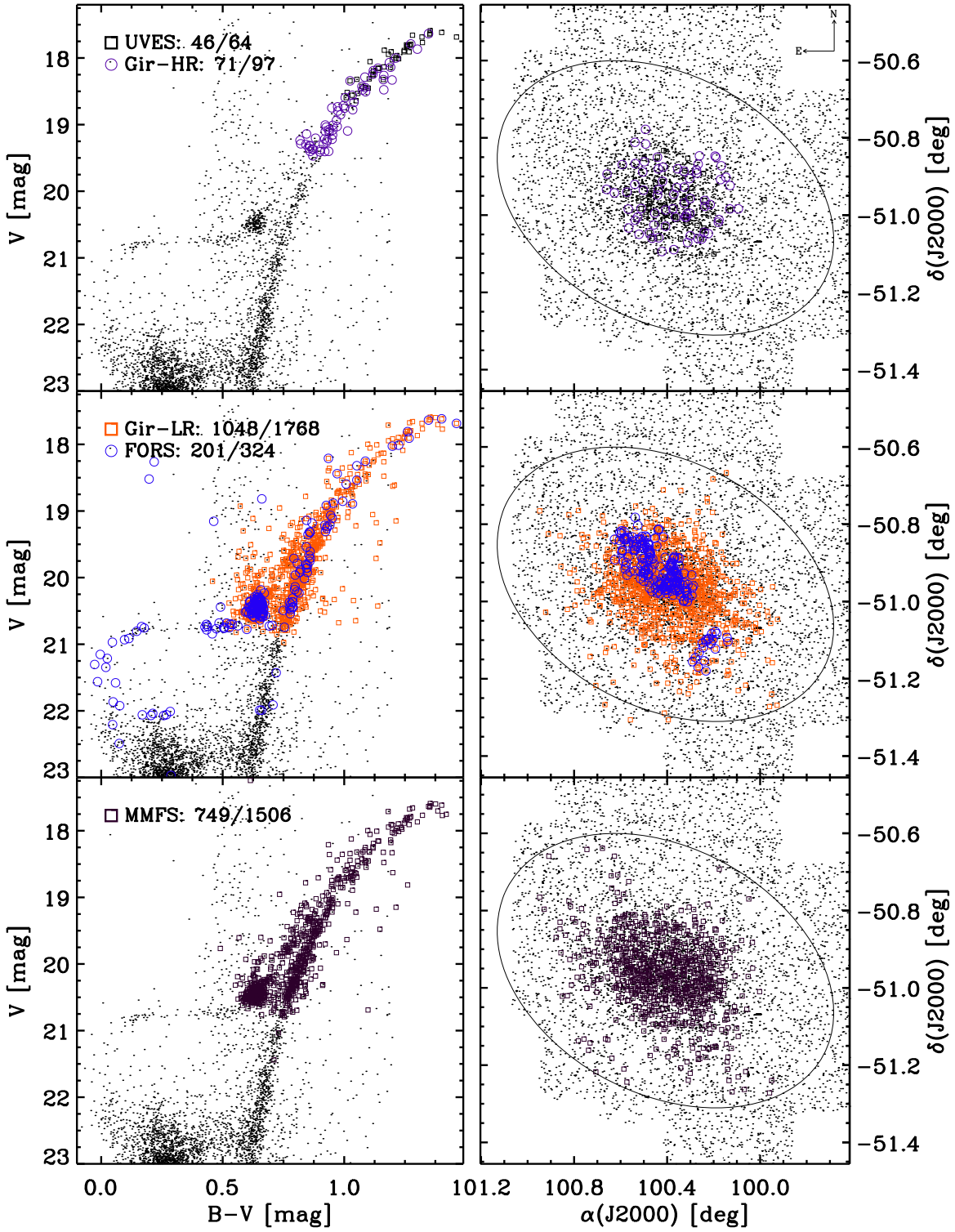


**Figure 1.** Left panels—distribution of the spectroscopic targets in the $V$ vs. $B$–$V$ color–magnitude diagram. From top to bottom targets with RV measurements based on high-resolution and medium-resolution spectra or available in the literature. Right panels—radial distribution of the spectroscopic targets overplotted on our Carina photometric catalog (black dots). The ellipse shows the Carina truncation radius.

presented here for the first time. The spectra were collected with VIMOS in service mode and Table 1 gives the log of the observations. The spectra were collected in good seeing conditions, and it is on average better than 1″ (see column 6) and with an airmass smaller than 1.″2. The spectra were collected with two pointings (see columns 2, 3, and 4) covering a substantial fraction of the body of the galaxy. The field of view of VIMOS is made by four quadrants of 7′ × 8′ each, separated by a cross-shaped gap that is ∼2′ wide. Special attention was paid to designing the masks of the individual pointings. We split them into deep and shallow masks. The former ones host in the four quadrants more than ∼150 slits, 0.″8 wide. The bulk of the targets of the deep masks are HB and RC stars. To improve the SNR of the faint targets, the same

**Table 1**
Log of VIMOS Observations

| Date | Pointing | $\alpha$(J2000) hh:mm:ss.ss | $\delta$(J2000) dd:mm:ss.s | Exp.Time s | Seeing[a] ″ | Airmass | Num. Slits |
|---|---|---|---|---|---|---|---|
| 2012 Dec 07 | Deep_North_1 | 06:42:27.93 | –50:56:25.5 | 2640 | 0.73-0.60 | 1.122 | 152 |
| 2012 Dec 23 | Deep_North_2 | 06:42:27.93 | –50:56:25.5 | 2640 | 0.75-0.65 | 1.166 | 152 |
| 2012 Dec 08 | Deep_North_3 | 06:42:27.93 | –50:56:25.5 | 2640 | 0.60-0.90 | 1.126 | 152 |
| 2012 Dec 09 | Deep_North_4 | 06:42:27.93 | –50:56:25.5 | 2640 | 1.12-0.73 | 1.127 | 152 |
| 2012 Dec 09 | Deep_North_5 | 06:42:27.93 | –50:56:25.5 | 2640 | 0.83-0.66 | 1.120 | 152 |
| 2012 Dec 23 | Deep_North_6 | 06:42:27.93 | –50:56:25.5 | 2640 | 0.54-0.60 | 1.118 | 152 |
| 2012 Dec 07 | Deep_North_7 | 06:42:27.93 | –50:56:25.5 | 2640 | 0.75-1.13 | 1.125 | 152 |
| 2012 Dec 31 | Deep_South_1 | 06:40:56.00 | –51:03:49.9 | 2640 | 0.75-0.67 | 1.174 | 161 |
| 2013 Jan 01 | Deep_South_2 | 06:40:56.00 | –51:03:49.9 | 2640 | 0.98-1.11 | 1.117 | 161 |
| 2013 Jan 01 | Deep_South_3 | 06:40:56.00 | –51:03:49.9 | 2640 | 1.20-1.38 | 1.153 | 161 |
| 2013 Jan 01 | Deep_South_4 | 06:40:56.00 | –51:03:49.9 | 2640 | 1.00-1.20 | 1.143 | 161 |
| 2013 Jan 02 | Deep_South_5 | 06:40:56.00 | –51:03:49.9 | 2640 | 0.75-0.82 | 1.250 | 161 |
| 2013 Jan 02 | Deep_South_6 | 06:40:56.00 | –51:03:49.9 | 2640 | 1.31-0.84 | 1.149 | 161 |
| 2013 Jan 02 | Deep_South_7 | 06:40:56.00 | –51:03:49.9 | 2640 | 0.76-0.66 | 1.117 | 161 |
| 2013 Jan 03 | Shallow_North_1 | 06:42:27.93 | –50:56:25.5 | 2640 | 0.90-1.11 | 1.121 | 107 |
| 2013 Jan 03 | Shallow_North_2 | 06:42:27.93 | –50:56:25.5 | 2640 | 1.16-0.84 | 1.176 | 107 |
| 2013 Jan 04 | Shallow_North_3 | 06:42:27.93 | –50:56:25.5 | 2640 | 0.93-0.96 | 1.116 | 107 |
| 2013 Jan 06 | Shallow_South_1 | 06:40:56.00 | –51:03:49.9 | 2640 | 0.69-0.85 | 1.131 | 110 |
| 2013 Jan 06 | Shallow_South_2 | 06:40:56.00 | –51:03:49.9 | 2640 | 0.90-0.99 | 1.119 | 110 |
| 2013 Jan 06 | Shallow_South_3 | 06:40:56.00 | –51:03:49.9 | 2640 | 0.84-0.82 | 1.167 | 110 |

**Note.**
[a] Seeing condition at the beginning and end of exposure.

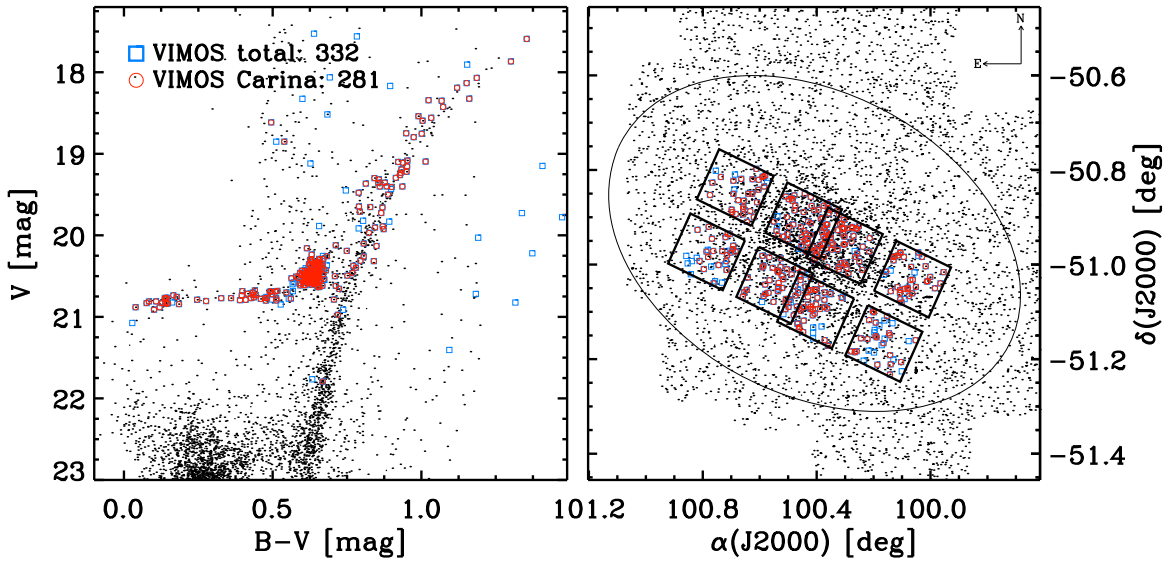


**Figure 2.** Same as Figure 1, but for the spectroscopic targets observed with VIMOS. Blue squares and red circles display candidate field and Carina stars. The black squares plotted in the right panel display the two VIMOS pointings (four chips each).

masks were repeated seven times; moreover, the two pointings partially overlap across the center of the galaxy (see the right panel of Figure 2). To improve the spatial sampling, the shallow masks cover the same sky area, the bulk of the targets are RG stars, and they typically host ∼110 slits, with similar slit width. These targets are brighter and the masks have only been repeated three times.

The faint sample covers a limited range in magnitudes ($20 \lesssim V \lesssim 21.5$ mag). This means the opportunity to properly trace old (blue and red HB stars) and intermediate-age (RC stars) stellar populations. These spectra also have a good overlap with both HR (15 objects) and MR (178 objects) spectra. The left panel of Figure 2 shows the distribution in the CMD of both the candidate field stars (cyan squares) and the candidate Carina stars (red circles), according to the kinematic selection. The right panel of the same figure shows the eight VIMOS pointings and the radial distribution of candidate field and galaxy stars.

### 2.1. VIMOS Spectra: Extraction and Wavelength Calibration

The observed spectra were individually extracted using the following approach. We wrote a custom software in *R* to extract the slits data from the bias corrected spectra, with the

associated flat and wavelamp.[16] The slit sky model was constructed via a row by row robust polynomial fit and then subtracted from the slit. The sky subtracted slits for the same target were combined using `imcombine` in IRAF.[17] The ensuing reference spectrum was extracted from the combined images using `apall` in IRAF. This reference spectrum was used to extract the single slit spectrum, which in turn, was also used as a reference in the `apall` procedure to extract the associated sky and the associated wavelength lamp. The wavelength calibration of the spectra was performed using `identify-reidentify` IRAF tasks. Subsequently, every sky spectrum was cross correlated with a synthetic sky radiance spectrum computed using SkyCalc and the shift in wavelength was applied to the target spectra.[18] To overcome possible systematics on RV measurements caused by non-optimal centering of the star in the slit, we cross correlated the star spectra with a synthetic sky transmittance spectrum over the wavelength range 7550–7750 Å, and the shift in wavelength applied accordingly. In particular, we used telluric absorption lines in the Fraunhofer A band (7167–7320 Å, 7593–7690 Å) to correct for possible star miscentering in slit (e.g., Sohn et al. 2007). A synthetic transmittance spectrum is cross correlated with the star spectrum, in the wavelength range of the Fraunhofer A band; essentially, the star is used as a lighthouse with the incoming light affected by the Earth also through atmospheric telluric absorption. The telluric feature positions and line shapes are pressure and wind dependent (e.g., Griffin 1973), however, they cause variations of the orders of tens of $m\,s^{-1}$ (i.e., well below the errors in our observations).

To validate the precision of the approach adopted to reduce and calibrate low-resolution spectra, the black dots plotted in Figure 3 show the VIMOS spectra of four stars ranging from a relatively bright Red Giant star (RG, $V = 17.74$ mag, panel (a)) to a fainter RC star (RC, $V = 20.27$ mag, panel (b)) and to even fainter red and blue HB stars (RHB, BHB, panels (c) and (d)) located at $V = 20.69$ and $V = 20.84$ mag. Note that the quoted figure shows the wavelength regions located around the strong H$\alpha$ line ($\lambda = 6562.8$ Å) and the regions around the Ca II triplet for cool and warm targets and the H-Paschen lines for the hotter RHB and BHB stars. This means that we can fully exploit the large wavelength range covered by VIMOS spectra in dealing with stars covering a broad range of effective temperatures and surface gravities.

To further constrain the plausibility of the current approach, Figure 3 also shows the comparison with synthetic spectra (red solid lines; see Section 3). To improve the precision of the RV velocity measurements, the synthetic spectra were degraded to the VIMOS spectral resolution using a Gaussian kernel and added noise to reach the typical signal-to-noise ratio of observed spectra. The main outcome is that the accuracy of the RV measurements based on VIMOS spectra range from better than $2\,km\,s^{-1}$ for the bright sources to better than $9\,km\,s^{-1}$ for the faintest sources in our sample. This evidence becomes even more compelling if we account for the total exposure time adopted, namely 7.5 hr per pointing and each pointing including, on average, 260 targets.

[16] https://cran.r-project.org

[17] IRAF is distributed by the National Optical Astronomy Observatory, which is operated by the Association of Universities for Research in Astronomy, Inc., under cooperative agreement with the National Science Foundation.

[18] www.eso.org/observing/etc/skycalc/skycalc.htm

## 3. RV MEASUREMENTS

The RV measurements were performed for each target on individual spectra, instead of measuring the RV of the co-added spectrum. The latter was the approach adopted in Fabrizio et al. (2011, 2012a) to determine the RV of both high-, medium-, and low-resolution spectra. The current measurements are based on a new procedure that performs an automatic cross-match between the observed spectrum and a synthetic one. The change in the data analysis strategy was motivated by the fact that the low-resolution spectra collected with VIMOS ($R \sim 600$) have a limited number of isolated and un-blended spectral features that can be safely adopted to provide accurate and precise RV measurements. The adopted synthetic spectra were extracted from the Pollux Database[19] (Palacios et al. 2010), with stellar parameters of typical RGB, RC, red HB, and blue HB stars. This means that we selected a grid of models with the following input parameters: $T_{\rm eff} = [5000, 5500, 6500, 7500]$ K, $\log g = [0.5, 2.5, 2.5, 2.5]$ dex, a stellar mass equal to 1 $M_{\odot}$, and spherical geometry. Moreover, the above models where computed at fixed chemical composition, $[{\rm Fe/H}] = -1.50$, and $[\alpha/{\rm Fe}] = +0.40$. Readers interested in a detailed discussion concerning the iron and the $\alpha$-element distribution of old- and intermediate-age subpopulations are referred to Fabrizio et al. (2015). The models were degraded to VIMOS spectral resolution using a Gaussian filter with the typical signal-to-noise ratio of observed data (~10–50). We performed a number of tests using models covering a broader range of input parameters, and we found that the RV measurements were minimally affected by plausible changes ($\Delta T_{\rm eff} = 300$ K, $\Delta \log g = 0.2$ dex, $\Delta[{\rm Fe/H}] = 0.2$) in the adopted synthetic spectra.

Specifically, the automatic procedure performs a Least Squares minimization of the residual between the observed spectrum and synthetic spectra. We performed a number of tests with medium- and high-resolution spectra degraded at the spectral resolution of VIMOS spectra, and we found that the typical precision of the current RV measurements is systematically better than $12\,km\,s^{-1}$ for both cool and warm targets.

### 3.1. Validation of RV Measurements

To validate the new RV measurements based on VIMOS spectra, we performed a series of comparisons with radial velocities measured on medium- and high-resolution spectra. The left side of panel (a) in Figure 4 shows a comparison between the VIMOS measurements and those based on high-resolution spectra (nine stars common) as function of the visual magnitude. The right side of the same panel displays the distribution of the residuals. The panel (b) displays a similar comparison and distribution as in panel (a), but for the 36 GHR stars in common. Although the number of objects in common is smaller than four dozen and relatively bright, the residuals are quite small and symmetric. The mean (biweight; Beers et al. 1990) difference is $<0.7\,km\,s^{-1}$, while the standard deviation is 7–8 $km\,s^{-1}$.

Panels (c) and (d) display the difference with radial velocities based on medium-resolution spectra (GMR, FORS2). The VIMOS sample has 178 stars in common with the GMR sample (black dots), and among them 166 stars are, according to the selection criteria discussed in Section 3.2, candidate

[19] pollux.graal.univ-montp2.fr

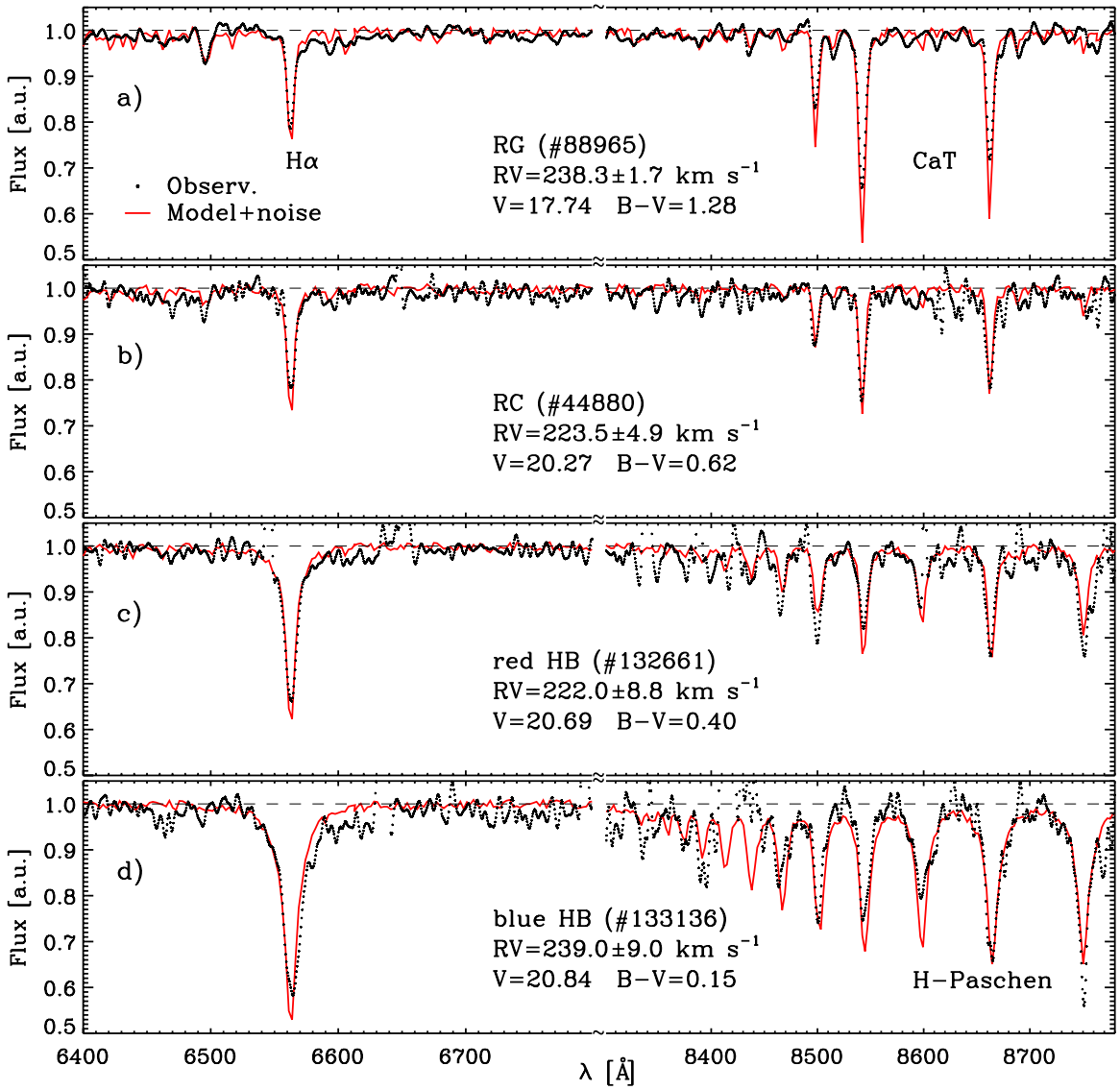


**Figure 3.** Panel (a)—Normalized VIMOS spectrum for a Red Giant (RG) star centered around the H$\alpha$ (left) and the Ca II triplet (right). The black dots display the observed spectrum, while the red line shows the synthetic spectrum. The number in parentheses shows the ID of the star in the photometric catalog. The radial velocity and its uncertainty is also labeled with the visual magnitude and the $B$–$V$ color of the target. Panel (b)—Same as Panel (a), but for a Red Clump (RC) star. Panel (c)—Same as Panel (a), but for a red HB star. Note that in the right portion of the spectrum the region around the hydrogen Paschen lines is shown. Panel (d)—Same as Panel (c), but for a blue HB star. See text for more details.

Carina stars (red dots). There are 43 objects in common with FORS2, and among them 41 are candidate Carina stars. In this case, the mean difference is on average of the order of 2 km s$^{-1}$, while the standard deviation is ∼15 km s$^{-1}$ (see labeled values for the different subsamples).

The last panel (e) shows the comparison between RV measurements based on VIMOS spectra and similar measurements available in the literature from Walker et al. (2007). The quoted sample has a large number of objects in common (i.e., 145 stars, ranging from the tip of the RGB down to RC stars). The mean difference is, once again, minimal (<1 km s$^{-1}$) and the residuals are symmetrical; this suggests the lack of systematics in radial velocities based on low-resolution VIMOS spectra.

It is noteworthy that the procedure we devised to calibrate VIMOS data, as described in Section 2.1, has substantially improved and reduced the differences between VIMOS radial velocities with similar measurements, but based on higher-resolution spectra (see Figure 4). In particular, the quoted differences increase by a factor of ten and the dispersion increases by a factor of three, if the wavelength calibration of VIMOS spectra was only based on lamps. The improvement mainly relies on the procedure adopted to extract and correct for slit centering (i.e., by performing the cross-match with radiance and transmittance sky spectra, respectively).

To further validate the RV measurements based on VIMOS spectra, and in particular the possible occurrence of systematics as a function of magnitude and spectral type, Figure 5 shows the RV errors ($\epsilon$RV) as function of both $V$ magnitude (panel (a)) and $B-I$ color (panels (b) and (c)). Note that to overcome the color overlap between the different stellar subgroups, panel (b)) mainly shows RGB stars brighter than $V\sim 20$ mag, while panel (c) mainly shows HB and RC stars fainter than $V\sim 20$ mag.

Data plotted in the quoted panels show no evidence of systematics in RV errors as a function of magnitude (panel (a)),

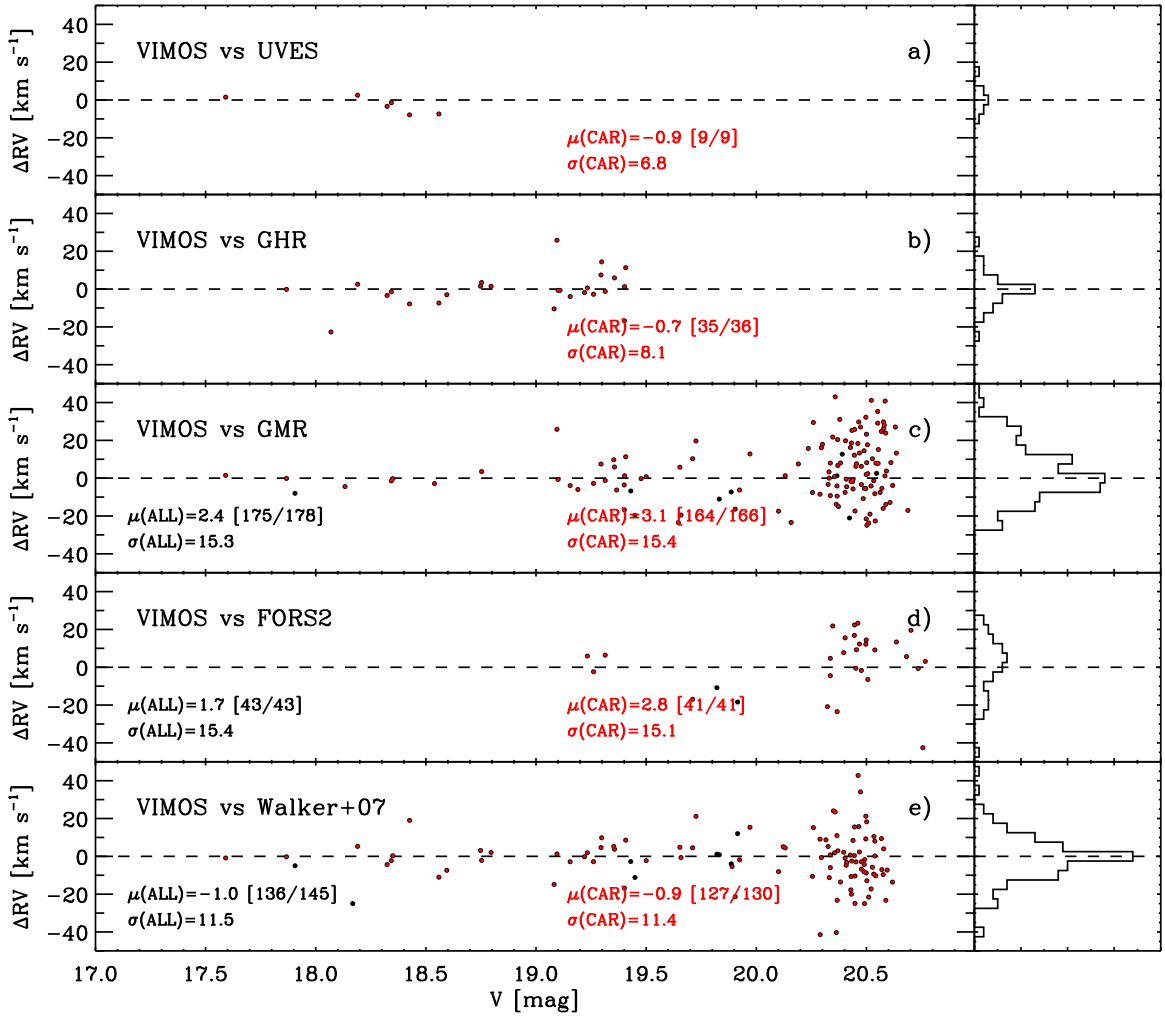


**Figure 4.** Comparison between RV measurements based on low-resolution spectra collected with VIMOS and literature estimates. The biweight mean ($\mu$), the standard deviation for the entire sample, and for the candidate Carina stars ($180 \leqslant$ RV $\leqslant 260$ km s$^{-1}$) are labeled. The numbers in brackets show the number of objects in common between the two samples before and after the biweight mean.

with a mean RV error for candidate Carina stars of 7.2 km s$^{-1}$, a velocity dispersion of 4.6 km s$^{-1}$, and the typical steady increase in the faint limit. The same outcome applies to the RV errors as a function of color (panels (b) and (c)), because their distribution, within the errors, is similar for blue ($B - I < 0.4$ mag) and red ($B - I > 1.5$ mag) spectroscopic targets. Moreover, the above results apply, as expected, to both field and galaxy stars. These finding allow us to end up with a robust and homogeneous catalog of RV measurements.

Table 2 lists the RV measurements of the entire spectroscopic sample. Columns 1–3 give the identity and coordinates of the stars, while columns 4–6 give the magnitudes in *V*, *B*, *I* and relative errors (from Bono et al. 2010; Stetson et al. 2011). The mean RVs are listed in column 7 with their measurement errors, while column 8 gives, for each target, the spectrographs adopted to collect the spectra. The last column lists a stellar population flag according to the *V* versus $c_{U,B,I}$ plane, and the CMD (see Figure 8).

The occurrence of binary stars among RG stars in dSph galaxies is a highly debated topic, and their impact on the RV dispersion ranges from a sizable effect (Queloz et al. 1995) to a modest error (Olszewski et al. 1996; Hargreaves et al. 1996) when compared with the statistical error. However, in a recent investigation, Minor et al. (2010) used a detailed statistical approach and found that dSph galaxies with RV dispersions ranging from 4 to 10 km s$^{-1}$ can be inflated by no more than 20% due to the orbital motion of binary stars. The key advantage of the current sample (Fabrizio et al. 2011) is that a significant fraction of stars have spectra collected on a time interval of more than 10 years. Therefore, the current RV measurements are less prone to significant changes caused by binary stars. Moreover, the conclusions of the current investigation are minimally affected by a possible uncertainty of the order of 20% in the RV dispersion.

### 3.2. RV Distribution

On the basis of our spectra (HR, MR, LR spectra), we ended up with homogeneous RV measurements for 2112 stars. The entire sample of RV measurements (ours, plus the literature) includes 2748 stars. We applied a $4\sigma$ selection criterium ($180 <$ RV $< 260$ km s$^{-1}$) and ended up with 1389 RV measurements of candidate Carina stars. The histogram plotted in the inset of Figure 6 shows the RV distribution of the candidate field and Carina stars. To overcome subtle problems in constraining the RV distribution caused by binning the data,

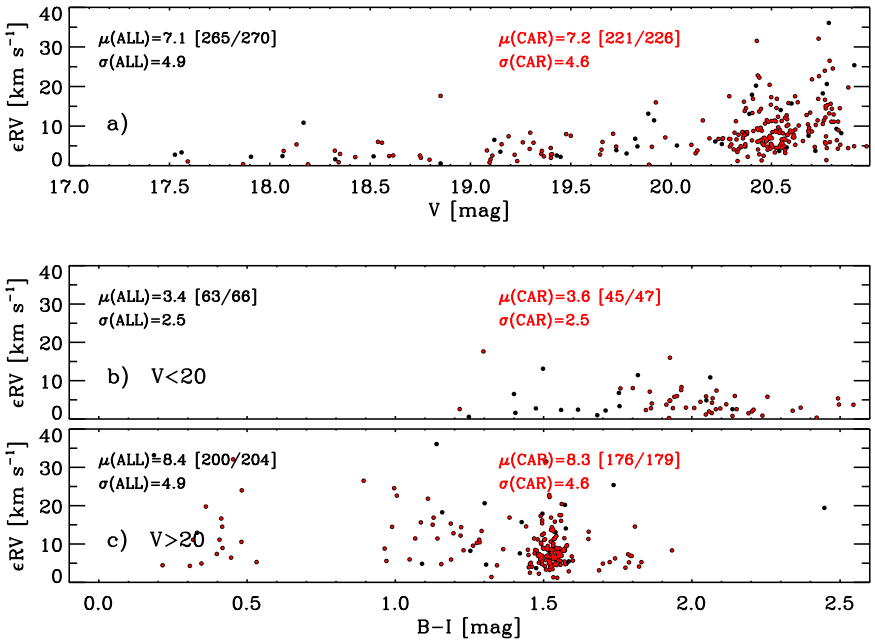


**Figure 5.** Radial velocity uncertainties ($\epsilon$RV) as function of $V$ magnitude (panel (a)) and $B - I$ color (panels (b) and (c)). In particular, panel (b) shows targets with $V < 20$ mag (mainly RGB stars), while panel (c) displays targets with $V > 20$ mag (HB and RC). The labels and numbers in parentheses have the same meaning as in Figure 4.

we assigned to each star a Gaussian kernel with a $\sigma$ equal to its intrinsic error on the RV measurement. The black solid curve was computed by summing all the Gaussians over the entire RV range. A glance at the quoted distribution shows a clear separation between candidate field and Carina stars. However, the criterium adopted for selecting candidate Carina stars, which was only based on the $\sigma$ of the RV distribution, might be affected by a bias. The high RV tail of the candidate field stars might attain RVs similar to Carina stars. To overcome this problem, we performed a global fit of the RV distribution using six Gaussians. The number and positions of the Gaussians are arbitrary, and they were selected to minimize the residuals over the entire velocity range. Among them, four were used to fit the RV distribution of candidate field stars, and two were used for the RV distribution of candidate Carina stars. Table 3 lists the adopted parameters for the multi-Gaussian fits.

To test the plausibility of the separation between the field and galaxy stars, the anonymous referee suggested comparing the current RV distribution with the Besançon Galaxy model[20] (Robin et al. 2003). We randomly extracted a number of stars similar to our sample of candidate field stars (~1360) from a complete simulation of 0.45 square degrees around the Carina coordinates. The same extraction was repeated 100 times to account for the limited area covered by the current spectroscopic sample, and we computed the mean RV distribution and standard deviation. Predictions from the Besançon Galaxy model were plotted as a gray shaded curve in Figure 6. The agreement between the theory and observations is quite good over the entire velocity range of field stars ($-20 \lesssim \mathrm{RV} \lesssim 180\,\mathrm{km\,s^{-1}}$). There is a mild excess of predicted stars in the low RV tail ($\mathrm{RV} \lesssim 30\,\mathrm{km\,s^{-1}}$), but this appears to be a minor problem, because we did not apply any local normalization. On the other hand, the predicted high tail vanishes for radial velocities that are larger than 150 $\mathrm{km\,s^{-1}}$. This suggestings that we are minimally overestimating the possible contamination of field stars within the main Carina peak. However, the above differences are within the current theoretical and empirical uncertainties (Czekaj et al. 2014).

To further constrain the quoted contamination, the left panel of Figure 7 shows a detail of the RV distribution across the Carina peak. The asymmetry in the Carina RV distribution was discussed by Fabrizio et al. (2011). Here we only mention that the main peak and $\sigma$ attain values ($220.74 \pm 0.28\,\mathrm{km\,s^{-1}}$, $\sigma = 10.5\,\mathrm{km\,s^{-1}}$) that agree quite well with previous estimates. Moreover, the individual Gaussians (see also Table 3) clearly indicate that the broad component is mainly responsible for the asymmetry in the RV distribution, while the narrow one is mainly shaping the RV peak. Once again, the number and the analytical functions adopted to perform the fit of the main peak are arbitrary and they were selected to minimize the residuals. The cyan area plotted in the bottom of the RV distribution shows the possible contamination of candidate Carina stars. We estimated a contamination of 135 field stars over a sample of 1389 candidate Carina stars. They were randomly extracted, and we ended up with a catalog of 1254 candidate Carina stars.

The right panel of Figure 7 shows the RV distribution of the candidate Carina stars after the subtraction of possible contaminants. We performed a series of Monte Carlo simulations in which we randomly extracted 135 contaminants from their candidate Carina stars. The RV distribution plotted in Figure 7 is the mean over 100 independent extractions. Note that both the global fit and the individual Gaussians, due to the sample size and RV precision, are minimally affected by the inclusion or exclusion of the possible contaminating field stars. The parameters of the final Gaussian fit are also listed in Table 3 with their uncertainties. The uncertainties are the standard deviations of the fits over 100 samples of cleaned RV distributions. In passing, we note that the broad and the narrow Gaussians display a difference in the peak of 1 $\mathrm{km\,s^{-1}}$, while the $\sigma$ of the former is almost a factor of two larger than the

[20] http://model.obs-besancon.fr

**Table 2**
Radial Velocities of Spectroscopic Targets

| ID | $\alpha$(J2000) deg | $\delta$(J2000) deg | $V$ mag | $B$ mag | $I$ mag | RV km s$^{-1}$ | Spect.[a] | Pop. Flag[b] |
|---|---|---|---|---|---|---|---|---|
| 107664 | 100.4775 | –50.9502 | 17.685 ± 0.003 | 19.147 ± 0.001 | 16.098 ± 0.003 | 230.1 ± 0.1 | 1, 3, 4 | 1 |
| 111206 | 100.4994 | –51.0315 | 17.702 ± 0.001 | 19.087 ± 0.001 | 16.146 ± 0.003 | 211.5 ± 1.5 | 3, 6 | 1 |
| 32411 | 99.98250 | –50.9602 | 17.883 ± 0.001 | 19.048 ± 0.004 | 16.464 ± 0.002 | 233.7 ± 0.1 | 1 | 1 |
| 78252 | 100.3008 | –51.2212 | 17.896 ± 0.001 | 19.119 ± 0.001 | 16.518 ± 0.004 | 234.4 ± 1.2 | 3, 6 | 1 |
| 102069 | 100.4432 | –51.0230 | 17.906 ± 0.001 | 19.152 ± 0.001 | 16.497 ± 0.001 | 213.0 ± 7.3 | 1, 3 | 1 |
| 107139 | 100.4744 | –50.9697 | 17.907 ± 0.001 | 19.100 ± 0.002 | 16.521 ± 0.001 | 216.8 ± 7.3 | 1 | 1 |

**Notes.**
[a] Adopted spectrographs: 1—UVES; 2—Gir-HR; 3—Gir-LR; 4—FORS2; 5—VIMOS; 6—MMFS.
[b] Stellar population flags: 0—Field candidates; 1—Old RGB candidates; 2—Intermediate RGB candidates; 3—Horizontal Branch; 4—Red Clump.
(This table is available in its entirety in machine-readable form.)

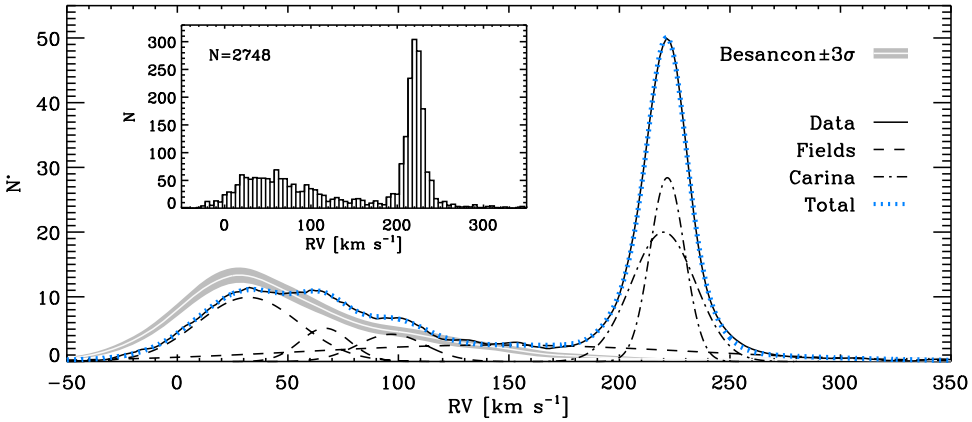


**Figure 6.** Global radial velocity distribution of the entire spectroscopic sample. The inset shows the histogram of the radial velocity measurements. The black solid line shows the smoothed radial velocity distribution using the Gaussian kernel. The dashed curves display the four Gaussians adopted to fit the candidate field stars, while the dashed-dotted curves show the two Gaussians adopted to fit the candidate Carina stars. The light blue dotted line shows the sum of the six Gaussians. The gray shaded curve shows the predicted mean radial velocity distribution, with the 3$\sigma$ error bar, based on the Besançon Galaxy model (see the text for more details, Robin et al. 2003).

**Table 3**
The Parameters of Multi-Gaussian Fit of the RV Distribution in the form: $y = A_0 \exp\left[-\frac{(x-\mu)^2}{2\sigma^2}\right]$

| Component | $A_0$ | $\mu$ (km s$^{-1}$) | $\sigma$ (km s$^{-1}$) |
|---|---|---|---|
| Field1[a] | 9.92 ± 0.02 | 32.12 ± 0.28 | 22.92 ± 0.21 |
| Field2[a] | 5.15 ± 0.08 | 66.76 ± 0.36 | 11.28 ± 0.32 |
| Field3[a] | 4.22 ± 0.02 | 96.86 ± 1.01 | 15.38 ± 0.63 |
| Field4[a] | 2.55 ± 0.01 | 145.09 ± 13.82 | 88.44 ± 6.45 |
| Carina_B[b] | 20.00 ± 0.16 | 219.93 ± 0.02 | 14.58 ± 0.03 |
| Carina_N[b] | 28.41 ± 0.22 | 221.67 ± 0.01 | 7.83 ± 0.01 |
| Carina_B-clean[c] | 16.05 ± 0.22 | 219.55 ± 0.05 | 15.98 ± 0.08 |
| Carina_N-clean[c] | 31.99 ± 0.30 | 221.58 ± 0.01 | 8.21 ± 0.01 |

**Notes.**
[a] Gaussians adopted to field the RV distribution of candidate field stars.
[b] Broad and narrow Gaussians adopted to fit the RV distribution of candidate Carina stars.
[c] Broad and narrow Gaussians adopted to fit the RV distribution of candidate Carina stars after the random cleaning of candidate field stars.

latter. This suggests that the two quoted components appear to trace stellar populations characterized by different kinematic properties.

In passing, we note that in a detailed photometric—based on DDO photometry—and spectroscopic investigation, Majewski et al. (2005) found evidence of possible contaminants from the Large Magellanic Cloud at radial distances of the order of few degrees from the Carina center. We did not check for these foreground stars because the current kinematic investigation is limited to stars located inside the Carina tidal radius. We plan to perform a detailed search for foreground stars and extra-tidal Carina stars (Muñoz et al. 2006) in a forthcoming investigation (M. Fabrizio et al. 2016, in preparation).

## 4. PHOTOMETRIC SELECTION

The optical $V$, $B-I$ color–magnitude diagram of Carina offers the opportunity to easily identify several evolutionary phases that can be associated either with the old (HB, subgiant branch [SGB]; plotted in red in the left panel of Figure 8) or the intermediate-age (RC, SGB; plotted in blue in the left panel of Figure 8). The two SGBs are too faint for the current 8–10 class telescopes. This is why we are only left with 74 HB and 414 RC stars as solid bright tracers of the old- and of the intermediate-age subpopulations. To further increase the sample of old- and intermediate-age stars, we took advantage of the new photometric index—$c_{U,B,I} = (U-B)$–$(B-I)$—introduced by Monelli et al. (2013). The index allows us, for the first time, to separate the two main subpopulations of

**Table 4**
The Biweighted Mean Radial Velocity (with error), Dispersion, and Number of Stars Values are Listed for the Total Sample, Intermediate-age, and Old Population

| Radius | Total | | | Interm. | | | Old | | |
|---|---|---|---|---|---|---|---|---|---|
| | RV (km s$^{-1}$) | $\sigma$ (km s$^{-1}$) | $N$ | RV (km s$^{-1}$) | $\sigma$ (km s$^{-1}$) | $N$ | RV (km s$^{-1}$) | $\sigma$ (km s$^{-1}$) | $N$ |
| ALL | 220.73 ± 0.28 | 10.51 | 1389 | 220.66 ± 0.30 | 9.88 | 1096 | 221.33 ± 0.75 | 12.91 | 293 |
| $r < r_c$ | 220.37 ± 0.36 | 9.91 | 748 | 220.29 ± 0.37 | 9.34 | 636 | 221.04 ± 1.27 | 13.42 | 112 |
| $r > r_c$ | 221.22 ± 0.44 | 11.23 | 638 | 221.21 ± 0.50 | 10.65 | 455 | 221.44 ± 0.94 | 12.65 | 181 |

**Note.** The rows refer to the entire spatial extension of spectroscopic targets, inside and outside the core radius ($r_c = 8\farcm8 \pm 1\farcm2$; Mateo 1998).

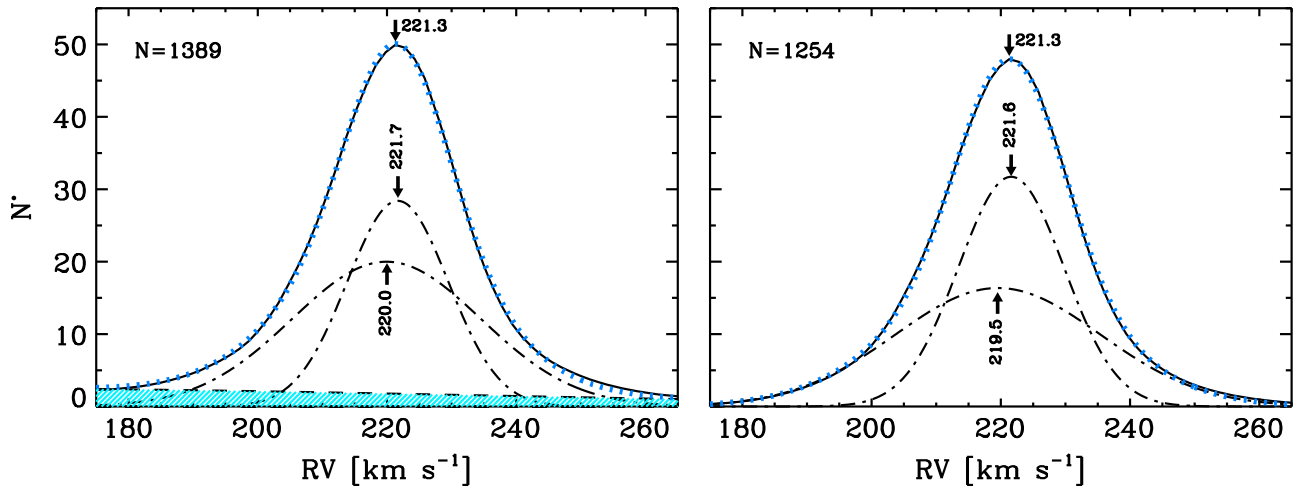


**Figure 7.** Left—Smoothed radial velocity distribution of candidate Carina stars (black curve). The dashed-dotted curves display the two Gaussians adopted to fit the RV distribution, while the light blue dotted curve shows their sum. The three arrows mark the peaks in radial velocity, and the values are also labeled (see also Table 3). The cyan area shows the possible overlap between the candidate field and Carina stars. Right—Same as the left panel, but after the random cleaning of field star contaminants (black curve). See text for more details.

Carina (old, intermediate-age) along a significant portion of the RGB (Monelli et al. 2014).

The right panel of Figure 8 shows the Carina brightest portion in the $V$, $c_{U,B,I}$ diagram. The colored symbols display the kinematical selected stars and the different colors are related to the different evolutionary phases and ages. The black dashed line shows the edge between the old (red) and intermediate-age (blue) RGB stars, and its location was fixed following Monelli et al. (2014). The red and blue symbols also mark the positions of the HB ($V = 20.75$, $c_{U,B,I} = -1.5/0$ mag) and RC ($V = 20.5$, $c_{U,B,I} = -1.6/-1.5$ mag) stars, respectively. The iso-contour of sky distributions for these two stellar components and the total sample are shown in Figure 9.

The link between the red and the blue RGB stars with the old and intermediate-age stellar population has been discussed in detail in Monelli et al. (2014) and Fabrizio et al. (2015). However, previous considerations were mainly based on photometric properties and leading evolutionary arguments concerning their distribution along the RGB and the ratio between the old and intermediate-age Carina stellar populations. Here, we take advantage of the new homogeneous and accurate RV measurements, including a sizable sample of solid tracers of the old stellar population, to further validate the $c_{U,B,I}$ index.

The top panel of Figure 10 displays the RV distribution of candidate intermediate-age RGB stars (blue shaded area), while the bottom panel shows the same distribution but for candidate old RGB stars. Quantitative constraints based on the $\chi^2$ of the two RV distributions indicate that they are different at the 99% confidence level. In particular, we found that the old component attains similar (after biweight cleaning) mean RV ($\mu \sim 221$ km s$^{-1}$), but larger RV dispersion ($\sigma = 11.7$ km s$^{-1}$) compared with the intermediate-age one ($\sigma = 9.7$ km s$^{-1}$). To further validate the above difference, we performed several numerical simulations in which we randomly extracted from the intermediate-age RGB subpopulation (682 stars) the same number of stars (219) included in the old RGB subpopulation. We found that the sample size does not affect the difference between the two subpopulations; the mean over the 100 experiments gives a mean RV of 220.6 km s$^{-1}$ and RV dispersion of 9.6 km s$^{-1}$. Interestingly, we found a similar difference in mean RV and RV dispersion values between HB stars (pure old component) and RC stars (pure intermediate-age component). The latter component has a mean RV of 219.9 km s$^{-1}$ and a RV dispersion of 10.2 km s$^{-1}$, while the former has 223.1 and 16.2 km s$^{-1}$, respectively. We performed a series of numerical experiments by randomly extracting 74 stars (HB stars) from the 414 RC stars, and we found very stable values for the mean RV and the RV dispersion (i.e., 220.1 and 10.0 km s$^{-1}$).

The current findings provide independent kinematic support for the connection between the red and blue RGB stars, selected according to the $c_{U,B,I}$ index, with old and intermediate-age stellar populations. In passing, we note that if the $c_{U,B,I}$ index in dwarf galaxies is mainly a metallicity indicator instead of an age indicator, the coupling of the more metal-poor subpopulation with old HB stars and of the more metal-rich subpopulation with RC stars is still in line with the kinematic analysis we plan to perform. The results of this investigation

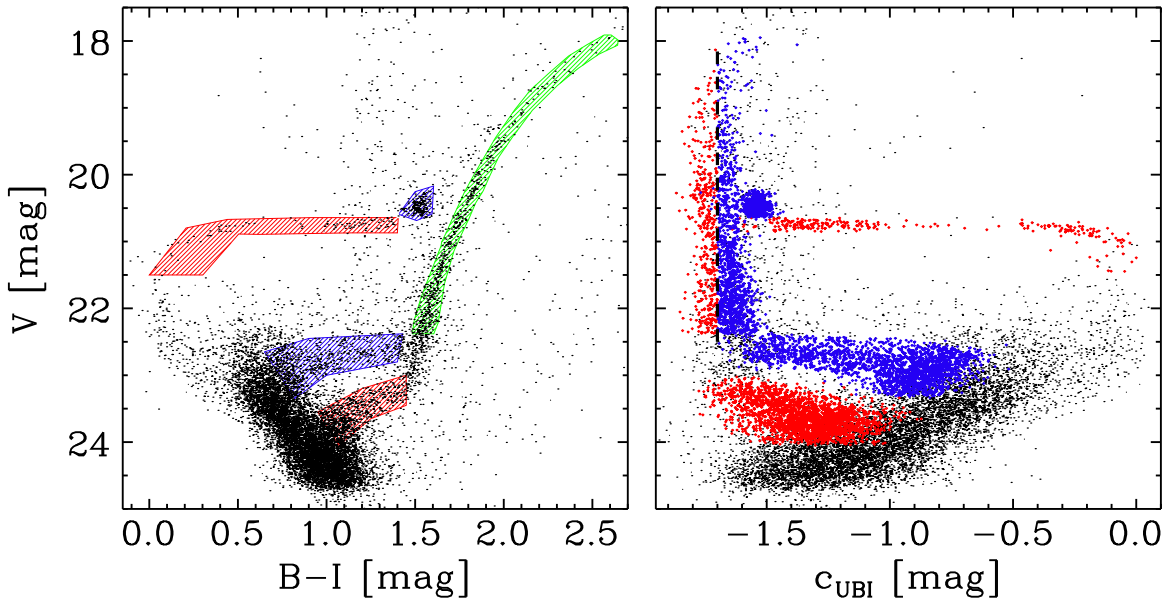


**Figure 8.** Left—Photometric selection of old (red) and intermediate-age (blue) candidate Carina stars based on the $V$ vs. $B - I$ CMD. The former included HB stars and faint subgiant branch stars, while the latter contained RC stars and bright subgiant branch stars. The green area shows RGB stars. Right—Same as the left panel, but in the $V$ vs. $c_{U,B,I}$ diagram. The vertical black dashed line shows the separation along the RGB between candidate old (red) and intermediate-age (blue) Carina stars. The old and the intermediate-age candidates selected in the left panel are also plotted with red and blue symbols.

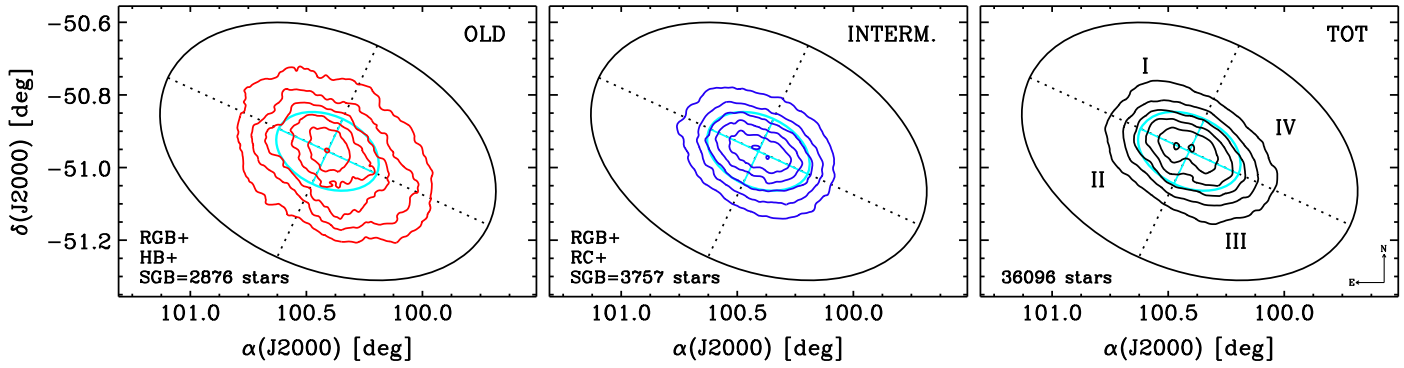


**Figure 9.** Isocontours of old (left, ∼2880 stars) and intermediate-age (middle, ∼3760 stars) stellar populations, selected using the photometric criteria shown in Figure 8. The black contours plotted in the right panel display the spatial distribution of the entire sample (36100) of candidate Carina stars (see, e.g., Bono et al. 2010). The cyan ellipse shows the Carina core radius. The adopted numbering for the quadrants is also labeled.

are not affected by the selection criteria adopted to separate the quoted subpopulations.

The above arguments are soundly supported by the clear difference in the sky distribution between the old tracers (red RGB, HB, faint SGB; 2876 stars) and the intermediate-age tracers (blue RGB, RC, bright SGB; 3757 stars). The former (left panel of Figure 9) is characterized by a broad radial distribution and by isocontours showing clear evidence of asymmetries when moving toward the outermost galaxy regions. The latter (middle panel) is more centrally concentrated and shows smoother radial distribution as a function of the radial distance. The isocontours of the entire sample of candidate Carina stars (right panel) show several secondary features (double peak, changes in the position angle), suggesting a more complex interaction among the different Carina subpopulations.

These findings fully support previous investigations concerning the difference between old and intermediate age stellar populations in Carina (Monelli et al. 2003) and dwarf spheroidals (Hidalgo et al. 2013; Monelli et al. 2016).

## 5. RV MAPS

The selection criteria described above allow us, for the first time, to handle a sizable sample of kinematic measurements of solid old candidate Carina stars (RGB+HB, 293 stars). The top-left panel of Figure 11 shows the RV map for the old stellar component. It was computed for every star in the sample by averaging over five nearest objects and smoothing with a Gaussian kernel in which the $\sigma$ was assumed to be equal to the RV dispersion of the five nearest stars. The RV map is color coded and the RV range is plotted on the right $y$-axis. To guide the reader, we overplotted the isophotal contours of the old candidate Carina stars on top of the RV map (see, Figure 9)

A preliminary analysis of the above maps suggests that the old subpopulation displays a RV distribution with a well-defined peak located across the innermost regions of the galaxy. The RV map does not show a clear pattern, and indeed kinematically hot and cold spots are present in the same quadrant. This notwithstanding, there is evidence of a well-defined increase in RV inside the core radius (see the solid semi-axis). Indeed these regions in the I, III, and IV quadrants

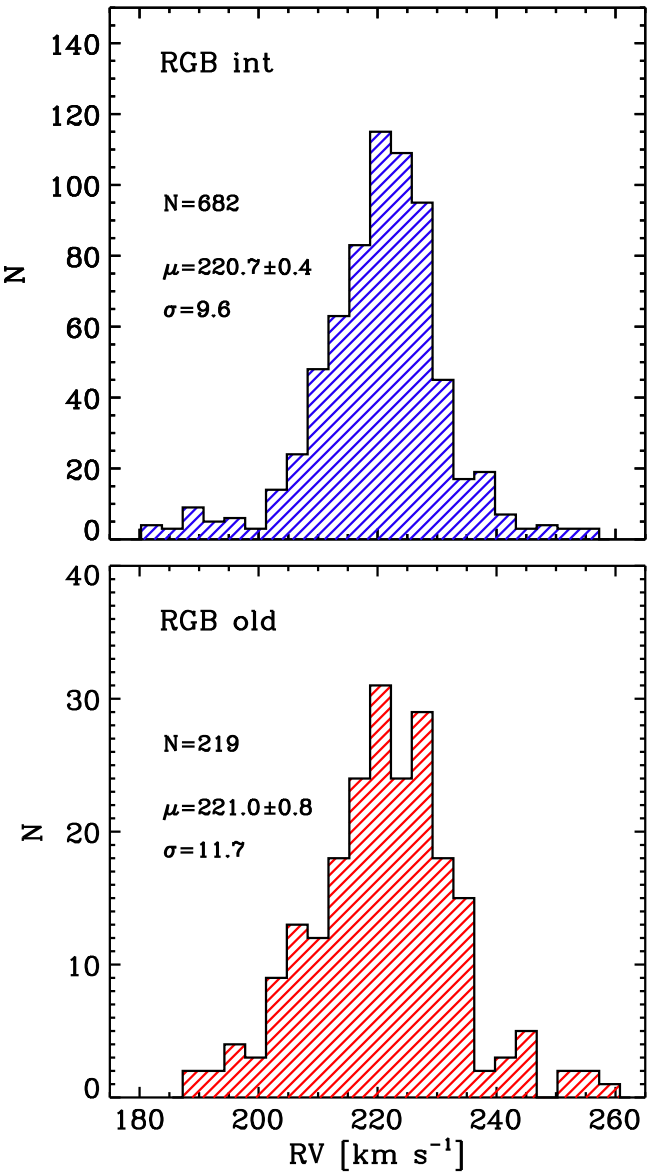


**Figure 10.** Top—RV distribution of candidate intermediate-age RGB stars. The number of stars, biweight mean (with error), and standard deviation values are also labeled. Bottom—Same as the top panel, but the red shaded area displays the candidate old RGB stars.

attain RVs that are either equal or larger than the peak in the RV distribution of the old subpopulation (221.3 km s$^{-1}$).

A similar RV map was also computed for the subpopulation of intermediate-age candidate Carina stars (RGB+RC, 1096 stars). The middle panel of Figure 11 shows the RV map computed by averaging the 25 nearest objects for every star in the sample. For the intermediate-age subpopulation we found clear evidence of an axial rotation. In particular, we found two well-defined regions covering the western (III and IV quadrants) and the eastern (I and II quadrants) sides of the galaxy, with a mean RV difference with respect to the RV peak of the intermediate-age subpopulation (220.7 km s$^{-1}$) of −4 km s$^{-1}$ and +5 km s$^{-1}$, respectively. We performed a number of tests to constrain the statistical significance of the above findings. In particular, we randomly extracted a subsample of ∼250 stars from the intermediate-age subsample, and once again computed the RV map. We found that the difference in RV pattern between the I+II quadrants and III +IV quadrants can be clearly detected in all of them. Note that the number of stars we randomly subtract from the intermediate-age subsample is similar to the size of the old age subpopulation. We changed the number of stars that were randomly subtracted from 1/4 to 1/3 of the entire sample, and we found once again the same RV pattern.

The top right panel of Figure 11 shows the RV map of the entire (old+intermediate-age) spectroscopic sample. The RV map is quite similar to the pattern shown by the intermediate-age subpopulation, suggesting that the global kinematical properties are mainly driven by this subpopulation. Note that the recent star formation history of this galaxy clearly indicates that the intermediate-age subpopulation includes the 70% of the entire stellar content of Carina (Small et al. 2013; de Boer et al. 2014; Savino et al. 2015).

The bottom left panel of Figure 11 shows the RV dispersion of the old subpopulation. Data plotted in this panel show three interesting features: (a) the old subpopulation attains RV dispersions that are, as expected, larger than the RV dispersion of the intermediate-age subpopulation. (b) The largest RV dispersions are approached in the same regions in which the RV map suggested a steady increase in RV distribution. Interestingly enough, values larger than 15 km s$^{-1}$ are attained in the I quadrant, in the regions located across the direction of the Carina proper motion (long blues arrows). However, the current uncertainties on the Carina proper motion do not allow us to constrain the above evidence. (c) There is evidence of a kinematically hot region in the first quadrant, for $\alpha = 6^{h}41^{m}54\overset{s}{.}60$ and $\delta = -50°53'6\overset{''}{.}9$, and of a cold region in the third quadrant. We double checked the radial distribution of the hot and cold regions and they appear real, because they are a mix of HB and old RGB stars. More firm conclusions require larger samples of old tracers.

The bottom middle panel of Figure 11 shows the RV dispersion of the intermediate-age subpopulation. The RV dispersion for this stellar component appears quite smooth and homogenous over the entire galaxy body. The RV dispersion of this stellar component is on average 50% smaller than the old subpopulations. The RV dispersion of the entire (old+intermediate-age, bottom right panel) spectroscopic sample is, once again, quite similar to the RV dispersion of the intermediate-age subpopulation.

To constrain the kinematic properties of the two quoted subpopulations on a more quantitative basis, we estimated their residual RV by subtracting to the entire RV map the peak of their RV distribution (i.e., the quantity $RV_{local\ mean}$–$RV_{Carina}$). In the following we define such a residual RV as "rotational velocity." The left panel of Figure 12 shows the ratio between the "rotational velocity" map and the RV dispersion map plotted in the bottom left panel of Figure 11 for the old, subpopulation. The range of values attained by the $V_{rot}/\sigma$ ratio are given on the the right $y$-axis. They are on average systematically smaller than 0.5, suggesting that the old subpopulation in Carina is pressure supported ($V_{rot}/\sigma < 1$) instead of rotation supported ($V_{rot}/\sigma > 1$). The same outcome applies to the intermediate-age population (middle panel) in which the ratio $V_{rot}/\sigma$ attains even smaller values. However, the asymmetry between the I+II and III+IV quadrants is still quite clear. The entire spectroscopic sample (right panel) shows, once again, a pattern that is similar to the intermediate-age subpopulation.

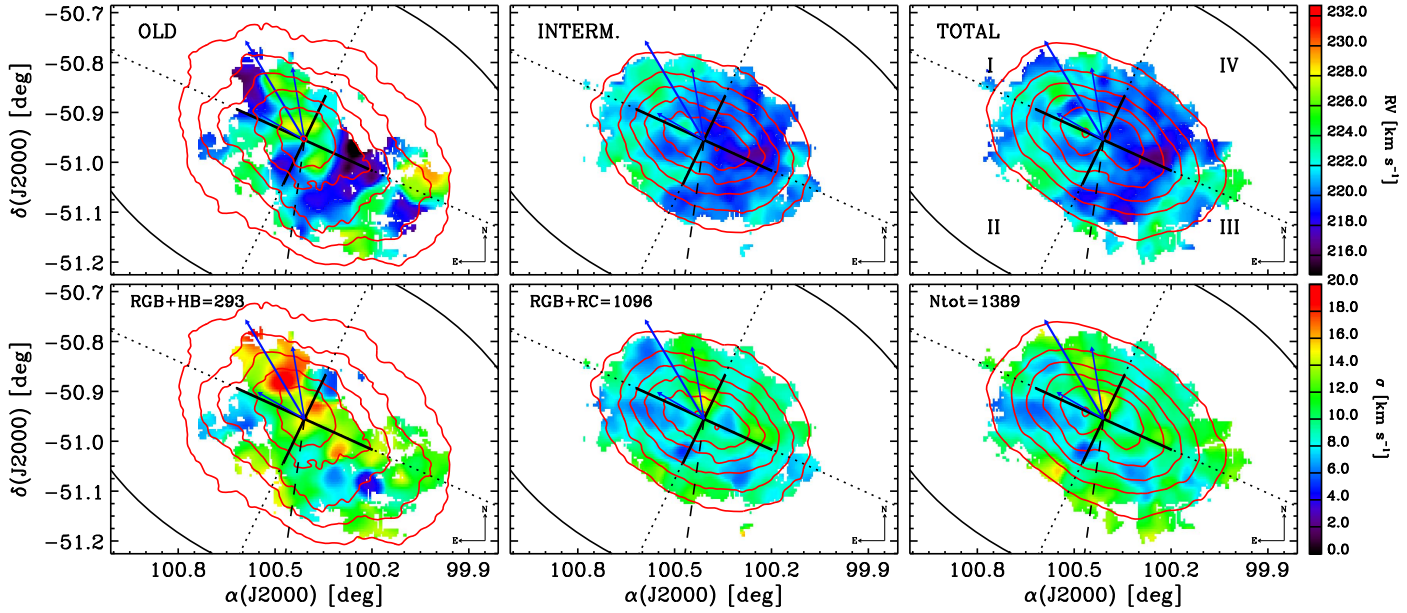


**Figure 11.** Top panels—Left: radial velocity map of the Carina old stellar population (HB, old RGB). The RV values were smoothed and color coded. Their range is plotted on the right *y*-axis. The black ellipse shows the Carina tidal radius, while the dotted lines show the major and the minor axis. The extension of the solid major and minor axis refers to the Carina core radius value (Mateo 1998). The red isocontours display radial distribution of the old stellar population selected using photometric criteria (see Figure 9). The arrows display the Carina proper motion and its uncertainty according to Metz et al. (2008) and S. Piatek (2016, private communication). The dashed black line shows the direction of the Galactic center. Middle: same as the left panel, but for the intermediate-age stellar population (RC, intermediate-age RGB). Right: same as the left panel, but for the entire spectroscopic sample. Bottom panels—Same as the top panels, but for the RV dispersion.

The above evidence indicates that Carina is mainly a pressure-supported stellar system. However, the occurrence of relic rotational map in the intermediate-age subpopulation seems to be supported by the RV map and the $V_{\rm rot}/\sigma$ map.

## 6. RV VARIATIONS

### 6.1. Radial Changes

To further constrain the kinematics of the Carina subpopulations, we decided to constrain the radial and the angular variations of both RV and RV dispersion. The top panel of Figure 13 shows the RV variation as a function of the radial Carina distance. Note that the radial distance was estimated taking into account the position angle and the eccentricity (see Fabrizio et al. 2011).

To avoid spurious fluctuations in the mean RV, we ranked the entire sample of old Carina stars as a function of the radial distance ($r$ (arcmin)) and estimated the running average by using the first 30 objects in the list. The mean distance and the mean velocity of the bin were estimated as the mean over the individual distances and RV measurements of the 30 objects included in the box. We estimated the same quantities moving by five objects in the ranked list until we accounted for the last five objects in the sample with the largest radial distances. The red shaded area shows the RV variation of the old subpopulation and takes into account the intrinsic errors in the RV measurements and in the possible field star contaminants. The approach adopted to constrain the latter uncertainty was already discussed in Section 5.

There is evidence that the RV of the old subpopulation after an initial increase in the innermost galactic regions ($r < 3'$) experiences a decrease of almost 8 km s$^{-1}$ when moving from $r \sim 3'$ to $r \sim 6'$. Moreover and even more important, the RV dispersion in the same regions decreases from ~15 km s$^{-1}$ to ~10 km s$^{-1}$. Thus suggesting a strong correlation with the RV variation. Estimates available in the literature suggest that the core radius of Carina is $r_c \sim 8\farcm8$ (Mateo 1998), however, the above evidence is suggestive of a more compact core region.

The RV of the old stellar component displays, at radial distances larger than the quoted secondary minimum, variations of the order of 2 km s$^{-1}$ up to $r \sim 15'$. At larger distances, the RV is steadily increasing until it approaches a broad secondary maximum (~225 km s$^{-1}$) and beyond a steady decrease until it approaches its absolute minimum (~215 km s$^{-1}$) in the outermost regions of the galaxy. The quoted radial variations indicate that $\sigma$ is almost constant over the entire region in which the RV shows the broad maximum. The RV and $\sigma$ approach their absolute minima toward the truncation radius of the galaxy ($r_t \sim 28\farcm8$).

The approach adopted to compute the mean RV of the intermediate-age population is the same as the old one, but the running average was computed including in the box 80 stars, and the box was moved in the ranked list of stars using 10 stepping stars. The blue shaded area plotted in Figure 13 shows the RV and the RV dispersion of the intermediate-age stellar component. The variation is smooth over the entire radial range covered by the current spectroscopic data. The variations in RV are on average smaller than 2 km s$^{-1}$, while the variations of the RV dispersion are smaller than 1 km s$^{-1}$. However, we do have evidence of a steady decrease in RV and of a steady increase in RV dispersion for radial distances larger than $r \sim 14'$. Note that these are the regions in which the old stellar component attains a broad maximum. Moreover, the $\sigma$ of the intermediate-age component for $r > 14'$ displays a mirror trend compared with the RV, because it steadily increases and attains its maximum value (~15 km s$^{-1}$) in the outermost galactic regions. The black shaded area display a similar trend, but in dealing with the entire sample we included 100 objects in the box and assumed 30 stepping stars. This is why the upper limit

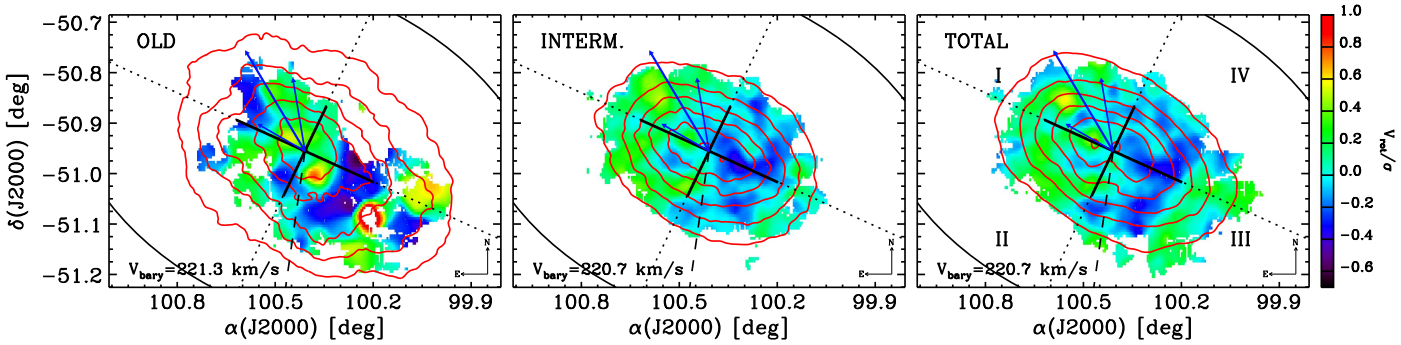


**Figure 12.** Left—RV map of the ratio between $V_{\rm rot}$ and RV dispersion for the old stellar population plotted in the right panels of Figure 11. The peak of the RV distribution adopted to estimate the $V_{\rm rot}$ is also labeled. Middle—Same as the left panel, but for the intermediate-age stellar population. Right—Same as the left panel, but for the entire spectroscopic sample.

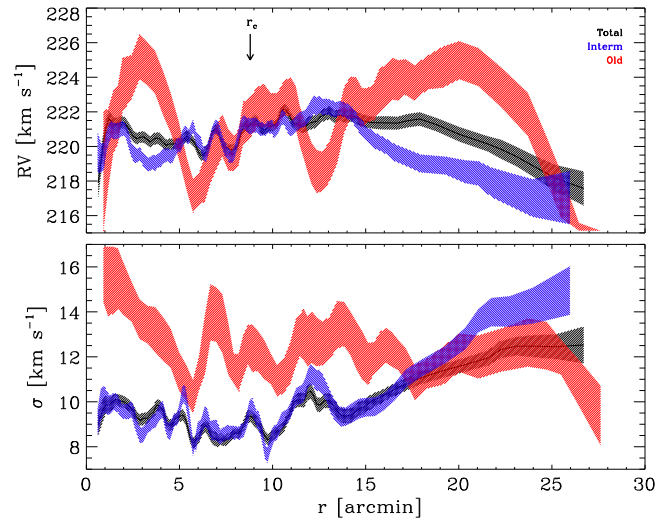


**Figure 13.** Top—Peak of the RV distribution as a function of the Carina galactocentric distance. The red stripe shows the RV for the old stellar population, while the blue one shows the RV for the intermediate-age and the black one shows the RV for the entire spectroscopic sample. The shaded areas take account of the uncertainties in RV distribution due to the random subtraction of contaminant field stars and RV measurements. The arrow marks the position of the Carina core radius. Bottom—Same as the top panel, but for the radial velocity dispersion.

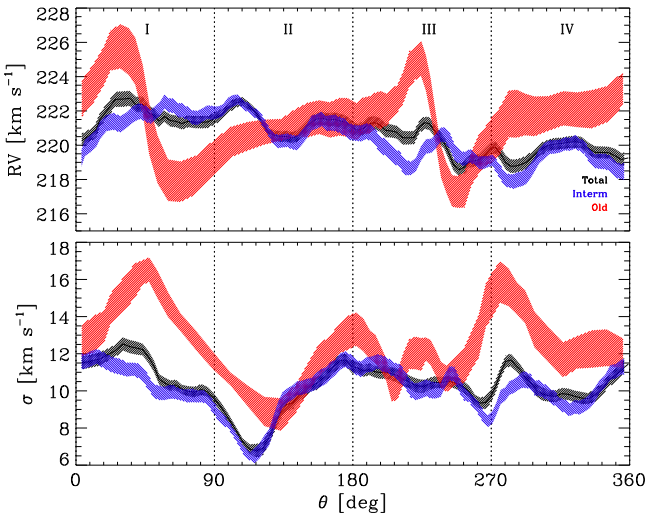


**Figure 14.** Same as Figure 13, but as a function of the angle across the Carina body.

in radial distance is between the old- and the intermediate-age stellar component.

### 6.2. Angular Changes

To further constrain the spatial variation in RV and RV dispersion, we also computed the running average as a function of the Carina angle. The main difference with the approach discussed in Section 6.1 is that we use a wedge instead of a box. We ranked the stars from the northern minor axis (0°) toward the eastern major axis (90°), and used the usual running average. For clearness, the quadrants were labeled as in Figure 9. The angular variations of both old- and intermediate-age subpopulations were estimated including the same number of stars and stepping stars that was adopted for the radial variations (see Section 6.1).

The shaded areas plotted in Figure 14 follow the same color code as in Figure 13. Data plotted in the top panel of Figure 14 display even more clearly that the old stellar component (red area) experiences significant changes in RV inside the I and III quadrants. The RV in the I quadrant moves from its absolute maximum to a secondary minimum, and the variation is of the order of 8 km s$^{-1}$; in the III quadrant it moves from a secondary maximum to its absolute minimum and the variation is quite similar. On the other hand, the RV in the II and IV quadrant shows a steady and smooth increase of a few km s$^{-1}$. The RV dispersion of the old subpopulation is also quite interesting, because it attains its absolute maximum and minimum ($\Delta\sigma \sim 7$ km s$^{-1}$) across the sharp variation in RV of the I quadrant ($50° < \theta < 140°$). On the other hand, the $\sigma$ variation across the sharp change in RV of the III quadrant ($200° < \theta < 250°$) is almost a factor of two smaller.

The intermediate-age stellar component (blue area) shows smooth variations across the four quadrants. There is evidence of a steady decrease of RV when moving from the I to the IV quadrant. The global variation is of order 5 km s$^{-1}$, with the absolute maximum located in the I quadrant and the absolute minimum in the IV quadrant. The RV dispersion shows a different trend, and indeed its entire excursion takes place inside the first two quadrants, where it changes from $\sim$12 km s$^{-1}$ at $\theta \sim 0°$ to $\sim$6 km s$^{-1}$ at $\theta \sim 120°$.

The above empirical evidence suggests that the sharp changes in RV and in $\sigma$ of the old subpopulation are taking place along the direction of the Carina proper motion. Once again the intermediate-age population appears reminiscent of a rotation pattern and the variations are smooth across the body of the galaxy.

## 7. COMPARISON WITH N-BODY SIMULATIONS

In this section we present a preliminary comparison of the observed RV distributions with *N*-body simulations described in Łokas et al. (2015). The velocity and dispersion maps of Figure 11 and the stellar density distributions of Figure 9 show very similar characteristics to the dwarf spheroidal galaxies formed as a result of tidal interactions of an initially disky dwarf galaxy orbiting a Milky Way–like host (e.g., see Figure 5 in Łokas et al. 2015 and Figure 15 in Ebrová & Łokas 2015). In this simulation (I0), the dwarf galaxy disk had an exactly prograde orientation with respect to the orbit, and the galaxy underwent a very strong transformation. At the first (out of five) pericenter passage the disk evolved into a bar, which during the subsequent evolution became shorter and thicker. For comparison with the data for Carina we used the simulation output saved after 8.5 Gyr from the start of the evolution, corresponding to the time after the fourth pericenter passage when the dwarf is at the apocenter of the orbit. At this time, most of the dwarf's initial rotation was already replaced by random motions and the simulated dwarf galaxy is approximately in equilibrium after being perturbed at the previous pericenter passage.

To properly compare theory and observations, the simulations were rescaled to the Carina distance ($D_\odot = 105 \pm 6$ kpc, Pietrzyński et al. 2009). Moreover, the Carina barycentric velocity (220.7 km s$^{-1}$) was also subtracted from the observed RV distribution. We investigated different lines of sight and the agreement between theory and observations was found to be best when the simulated dwarf galaxy was observed at an angle of 60° with respect to the major axis of the stellar component, but keeping the observer on the orbital plane of the dwarf.

We constructed the RV maps of the simulated dwarf following the same approach adopted for measuring the RV distribution (Figure 11) and the RV dispersion (Figure 12) of the observations. We randomly selected from the simulations a subsample of 2000 stars (i.e., a number of objects similar to the observed sample). To account for instrumental errors, the predicted RV measurements were convolved with a Gaussian distribution with a $\sigma$ of 4 km s$^{-1}$. Figure 15 shows, from top to bottom, the maps for the rotational velocity, the velocity dispersion, and the $V_{\rm rot}/\sigma$ ratio for the selected simulation output. On top of the above maps, we also plotted the surface density contours calculated from a larger sample of 36,000 stars, corresponding to the number currently available in photometric studies. Figure 16 shows the comparison between the rotational velocity, the velocity dispersion, and the $V_{\rm rot}/\sigma$ ratio measured in the core along the major axis of both the simulated and the real dwarf.

Given that the simulation discussed here was not performed to reproduce the observed properties of Carina, the similarity of the mock velocity maps and profiles to the real data for Carina is astonishing. The comparison strongly argues for a formation scenario in which Carina started as a disky dwarf and experienced strong, possibly multiple, tidal interactions with the Milky Way. As a result, it transformed from a disk to a prolate spheroid, and its rotation was replaced by random motions. However, some residual rotation around the minor axis remained as a relic of its initial conditions. For this process to be efficient, Carina must have been accreted on a prograde, rather than a retrograde orbit (Łokas et al. 2015). We performed several numerical experiments using *N*-body simulations with different initial conditions (prograde, retrograde orientations) and different epochs after starting their evolution. In some cases we found a good match either of the shape (I90) or of the $V_{\rm rot}/\sigma$ ratio (I270). However, the best fit of both the shape and the kinematics is only obtained for the above prograde orbit.

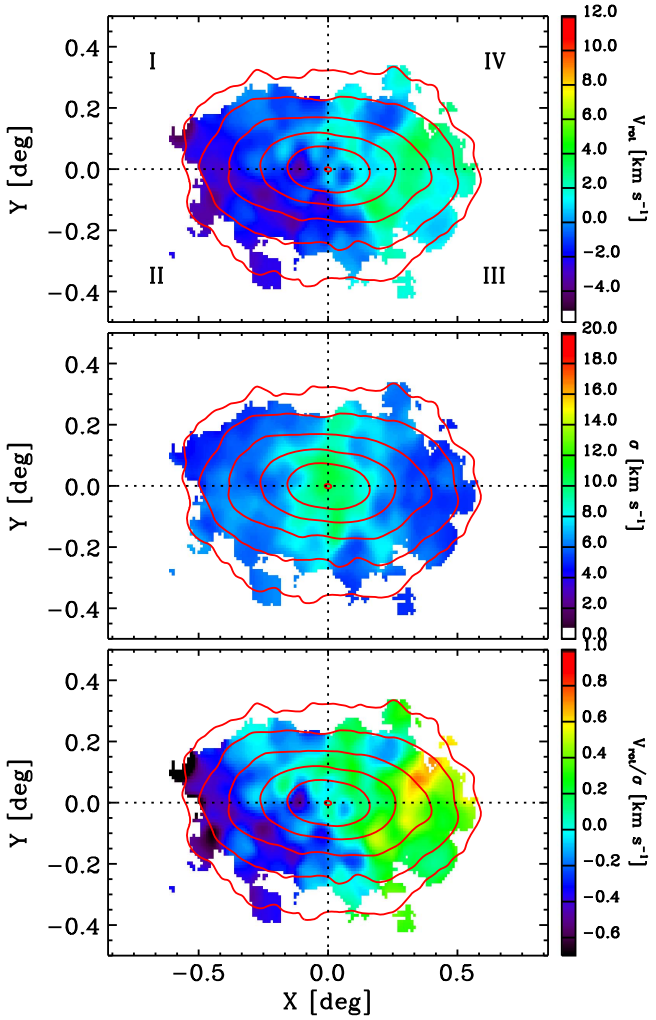


**Figure 15.** Top—Rotational velocity map based on the *N*-body model (view angle of 60° with respect to the major axis). The criteria adopted to select predicted velocities are discussed in detail in the text. Middle—Same as the top panel, but for the velocity dispersion. Bottom—Same as the top panel, but for the $V_{\rm rot}/\sigma$ ratio.

## 8. SUMMARY AND FINAL REMARKS

We present new RV measurements of Carina evolved stars using optical low-resolution spectra ($R \sim 600$) collected with VIMOS, a multiobject slit spectrograph available at the VLT. The spectra were collected using the MR-GG475 grism, with a wavelength coverage of 4800 ÷ 10,000 Å. We secured, with ~15 hr of exposure time, 2454 individual spectra for 332 stars. The targets have visual magnitudes ranging from $V = 20$ to $V = 21.5$ mag, and they are either old HB stars or intermediate-age RC stars or RGB stars. The new data were complemented with archival optical medium- and high-resolution spectra collected with FORS2 ($R \sim 2500$), GIRAFFE-LR ($R \sim 6500$), GIRAFFE-HR ($R \sim 20{,}000$), and UVES ($R \sim 40{,}000$) spectrographs at VLT. The spectroscopic data were collected on a time interval of 12 years. We ended up with a sample of more than 21,000 spectra for 2112 stars.

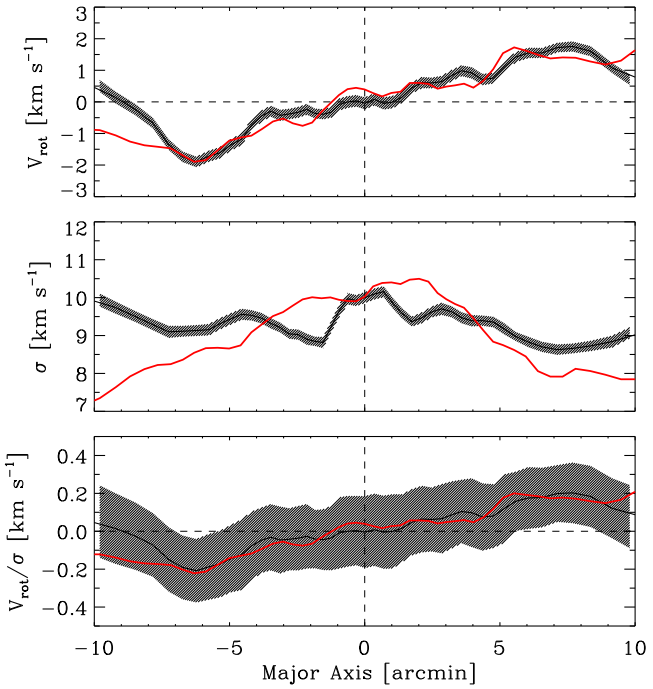


**Figure 16.** Top—Comparison between the predicted (red line) and observed (black line) rotational velocity, measured along the major axis of the Carina central regions. Middle—Same as the top panel, but for the velocity dispersion. Bottom—Same as the top panel, but for the $V_{\rm rot}/\sigma$ ratio.

The above data were complemented with RV measurements for more than 1500 stars available in the literature and based on high-resolution spectra (Walker et al. 2007). As a whole, we have RV measurements for 2748 stars and among them 1389 are candidate Carina stars. The current spectroscopic data set covers the entire body of the galaxy, with the high-resolution spectra that are more centrally concentrated, while medium- and low-resolution spectra approach the truncation radius.

Special attention was paid in the validation of RV measurements among the different spectroscopic samples. Moreover, the sizable sample of targets in common allowed us to perform an accurate calibration of radial velocities based on low-resolution spectra.

We also took advantage of the superb multiband (*UB VI* ) photometric catalog that our team collected during the last 20 years, and in particular, of the $c_{\rm U,B,I}$ index to select candidate old and intermediate-age subpopulations.

Interestingly enough, we found that the RV distributions of "cooler" and "hotter" (according to the $c_{\rm U,B,I}$ index) RGB stars attain dissimilar values for (biweight) mean RV and dispersion, and they are different at the 99% confidence level. On the other hand, the distribution of "hotter" RGB stars shows a standard deviation similar to the distribution of RC stars, which are intermediate-age tracers. The same occurs between the distributions of "cooler" RGB and HB stars, which are old stellar tracers. This provides independent kinematic support to the use of $c_{\rm U,B,I}$ as either an age and/or a metallicity indicator.

The photometric and kinematic selections allowed us to build a sample of ∼300 old (HB+RGB) and ∼1100 intermediate-age (RC+RGB) stellar tracers. The RV distribution of the old subpopulation attains peaks inside and outside the core radius that are slightly larger than the intermediate-age subpopulation, but the difference is smaller than $1\sigma$. However, the standard deviation of the former sample is systematically larger (2–3 km s$^{-1}$) than the latter one. The RV map of the old subpopulation does not show evidence of a pattern, instead it is characterized by an uneven distribution of hot and cold spots across the body of the galaxy. The RV dispersion attains values larger than 15 km s$^{-1}$ in the direction of the Carina proper motion. However, the current uncertainties on proper motion do not allow us to constrain this empirical evidence.

The RV map of the intermediate-age subpopulation shows evidence of an axial rotation between the western (III and IV quadrant) and the eastern (I and II quadrant) sides of the galaxy. The difference in RV between the main peak and the above regions is of –4 and +5 km s$^{-1}$. The RV dispersion of the intermediate-age subpopulations has a smooth variation across the entire body of the galaxy. Inside the core radius it is roughly 50% smaller than the RV dispersion of the old stellar component.

The RV maps were also adopted to estimate the rotation velocity (i.e., the difference between the local value of the RV and the main peak of the Carina RV distribution). We found that both the old and the intermediate-age subpopulations attain values of the $V_{\rm rot}/\sigma$ ratio that are systematically smaller than one, thus suggesting that Carina is a pressure-supported instead of a rotation-supported stellar system.

The kinematics of the old subpopulation show a complex variation as a function of the radial distance. The RV and the RV dispersion displays their entire excursion inside the core radius. The same parameters show changes of the order of 2 km s$^{-1}$ in the outermost regions, and attain their absolute minima across the truncation radius. On the other hand, the intermediate-age subpopulation shows smooth radial variations; but for radial distances larger than 15′ the RV is steadily decreasing by more than 3 km s$^{-1}$, while the RV dispersion is steadily increasing by more than 4 km s$^{-1}$.

The old stellar component also shows a complex angular variation. It experiences significant variations in the I and III quadrants with RV that change inside the above gradients by ∼8 km s$^{-1}$. The RV dispersion shows similar variations in the I quadrant, but they are significantly smaller in the III one. Firm conclusions concerning the difference do require larger samples of the old subpopulation. The intermediate-age stellar component shows, once again, smooth angular variations. It is worth mentioning that the RV dispersion of this subpopulation shows a trend that is similar to the old subpopulations in the first two quadrants. However, both the absolute maximum and the absolute minimum do not appear to be symmetric, and indeed the extrema of the former component anticipate the latter ones.

In order to provide more solid constraints on the kinematical structure of Carina, we performed a detailed comparison between observed and predicted RV distributions based on *N*-body simulations for a former disky dwarf galaxy orbiting a giant Milky Way–like galaxy recently provided by Łokas et al. (2015). In comparison with Carina, we selected a simulation in which the dwarf galaxy disk had a prograde orientation with respect to its orbit and 8.5 Gyr after the start of its evolution (i.e., after its fourth pericenter passage). We found that the best fit between theory and observations is attained when the simulated galaxy is viewed at an angle of 60° with respect to its major axis.

The values attained by the predicted $V_{\rm rot}/\sigma$ ratio are in remarkable agreement with the observations over the central regions of the galaxy ($-10' \lesssim r \lesssim 10'$). This finding becomes even more compelling if we account for the fact that the

adopted theoretical framework is not specific for Carina. Moreover and even more important, it strongly suggests that the current Carina dSph was a disky dwarf galaxy that underwent several strong tidal interactions with the Milky Way. These interactions transformed Carina from a disky to a prolate spheroid, and its rotational velocity was steadily transformed into random motions. The rotational velocity we detected along the major axis is still a relic of its initial conditions.

Our findings make Carina an excellent example of the process of the formation of dwarf spheroidal galaxies via tidal stirring of disky dwarfs. This argument is further supported by the fact that recent estimates indicate that the Carina kinematics are strongly dominated by its DM halo. Indeed, Łokas (2009), using the RV distribution provided by Walker et al. (2009a) and assuming that mass follows light, found a mass-to-luminosity ratio $M/L = 66 \pm 31$ (solar units). The above hypothesis that mass follows light is quite plausible for strongly tidally stirred stellar systems like Carina, because the DM halo is trimmed down and it does not extend well beyond the stellar component.

The increase in the sample size and the spatial sampling is suggesting an increase in the RV dispersion. This would imply a steady increase in the $M/L$ ratio. However, current findings are suggesting that the RV dispersion of the old stellar component is systematically larger than the RV dispersion of the intermediate-age component. The latter sample accounts for at least two-thirds of the Carina stellar content, thus suggesting that detailed knowledge of the kinematics of the different stellar components is mandatory to constrain the $M/L$ ratio of nearby stellar systems. The increase in sample size and spatial coverage implies a steady decrease in the sampling error associated with the $M/L$ ratio.

In a forthcoming investigation, aimed at specifically reproducing Carina, we will use *N*-body simulations including gas dynamics and star formation to model different stellar populations, as well as the known constraints on the Carina's orbit to study the possible contamination from the tidal tails (Klimentowski et al. 2007, 2009). This is an ambitious project because it requires a substantial improvement in the sample size of the old stellar component and in the galaxy regions located across and beyond the truncation radius. The observing and data reduction strategy we devised with VIMOS appears a very good viaticum. It goes without saying that the use of the ground layer adaptive optics facility at UT4 of VLT (GRAAL, Siebenmorgen et al. 2011) and the new integral field spectrograph MUSE (Bacon et al. 2006) will also open new paths in constraining the kinematic properties of nearby dwarf galaxies.

It is a pleasure to acknowledge the anonymous referee for her/his comments and suggestions that improved the content and the readability of our manuscript. MF acknowledges financial support from the PO FSE Abruzzo 2007–2013 through the grant "Spectro-photometric characterization of stellar populations in Local Group dwarf galaxies" prot.89/2014/OACTe/D (PI: S. Cassisi). GB thanks the Japan Society for the Promotion of Science for a research grant (L15518). MN acknowledges support from PRIN-INAF 2014 1.05.01.94.02. ELŁ acknowledges support of the Polish National Science Center under grant 2013/10/A/ST9/00023.

*Software:* R, IRAF, IDL.

## REFERENCES

Appenzeller, I., Fricke, K., Fürtig, W., et al. 1998, Msngr, 94, 1
Bacon, R., Bauer, S., Böhm, P., et al. 2006, Msngr, 124, 1
Beers, T. C., Flynn, K., & Gebhardt, K. 1990, AJ, 100, 32
Bono, G., Stetson, P. B., Walker, A. R., et al. 2010, PASP, 122, 651
Carney, B. W., & Seitzer, P. 1986, AJ, 92, 23
Czekaj, M. A., Robin, A. C., Figueras, F., Luri, X., & Haywood, M. 2014, A&A, 564, A102
de Blok, W. J. G. 2010, AdAst, 2010, 789293
de Boer, T. J. L., Tolstoy, E., Lemasle, B., et al. 2014, A&A, 572, A10
Dekker, H., D'Odorico, S., Kaufer, A., Delabre, B., & Kotzlowski, H. 2000, Proc. SPIE, 4008, 534
Ebrová, I., & Łokas, E. L. 2015, ApJ, 813, 10
Fabrizio, M., Ferraro, I., Iannicola, G., et al. 2012a, JPhCS, 383, 012009
Fabrizio, M., Merle, T., Thévenin, F., et al. 2012b, PASP, 124, 519
Fabrizio, M., Nonino, M., Bono, G., et al. 2011, PASP, 123, 384
Fabrizio, M., Nonino, M., Bono, G., et al. 2015, A&A, 580, A18
Griffin, R. 1973, MNRAS, 162, 243
Hargreaves, J. C., Gilmore, G., & Annan, J. D. 1996, MNRAS, 279, 108
Hidalgo, S. L., Monelli, M., Aparicio, A., et al. 2013, ApJ, 778, 103
Klimentowski, J., Łokas, E. L., Kazantzidis, S., et al. 2007, MNRAS, 378, 353
Klimentowski, J., Łokas, E. L., Kazantzidis, S., et al. 2009, MNRAS, 400, 2162
Kormendy, J., & Freeman, K. C. 2004, in IAU Symp. 220, Dark Matter in Galaxies, ed. S. Ryder et al. (San Francisco: Astronomical Society of the Pacific), 377
Le Fèvre, O., Saisse, M., Mancini, D., et al. 2003, Proc. SPIE, 4841, 1670
Leaman, R., Venn, K. A., Brooks, A. M., et al. 2013, ApJ, 767, 131
Łokas, E. L. 2009, MNRAS, 394, L102
Łokas, E. L., Semczuk, M., Gajda, G., & D'Onghia, E. 2015, ApJ, 810, 100
Majewski, S. R., Frinchaboy, P. M., Kunkel, W. E., et al. 2005, AJ, 130, 2677
Majewski, S. R., Ostheimer, J. C., Patterson, R. J., et al. 2000, AJ, 119, 760
Mateo, M., Nemec, J., Irwin, M., & McMahon, R. 1991, AJ, 101, 892
Mateo, M., Olszewski, E. W., Pryor, C., Welch, D. L., & Fischer, P. 1993, AJ, 105, 510
Mateo, M., Olszewski, E. W., & Walker, M. G. 2008, ApJ, 675, 201
Mateo, M. L. 1998, ARA&A, 36, 435
Metz, M., Kroupa, P., & Libeskind, N. I. 2008, ApJ, 680, 287
Minor, Q. E., Martinez, G., Bullock, J., Kaplinghat, M., & Trainor, R. 2010, ApJ, 721, 1142
Monelli, M., Gallart, C., Hidalgo, S. L., et al. 2010a, ApJ, 722, 1864
Monelli, M., Hidalgo, S. L., Stetson, P. B., et al. 2010b, ApJ, 720, 1225
Monelli, M., Martínez-Vázquez, C. E., Bernard, E. J., et al. 2016, ApJ, 819, 147
Monelli, M., Milone, A. P., Fabrizio, M., et al. 2014, ApJ, 796, 90
Monelli, M., Milone, A. P., Stetson, P. B., et al. 2013, MNRAS, 431, 2126
Monelli, M., Pulone, L., Corsi, C. E., et al. 2003, AJ, 126, 218
Muñoz, R. R., Majewski, S. R., Zaggia, S., et al. 2006, ApJ, 649, 201
Navarro, J. F., Frenk, C. S., & White, S. D. M. 1997, ApJ, 490, 493
Olszewski, E. W., Pryor, C., & Armandroff, T. E. 1996, AJ, 111, 750
Palacios, A., Gebran, M., Josselin, E., et al. 2010, A&A, 516, A13
Pasquini, L., Avila, G., Blecha, A., et al. 2002, Msngr, 110, 1
Pietrzyński, G., Górski, M., Gieren, W., et al. 2009, AJ, 138, 459
Queloz, D., Dubath, P., & Pasquini, L. 1995, A&A, 300, 31
Robin, A. C., Reylé, C., Derriére, S., & Picaud, S. 2003, A&A, 409, 523
Sanna, N., Bono, G., Stetson, P. B., et al. 2010, ApJL, 722, L244
Savino, A., Salaris, M., & Tolstoy, E. 2015, A&A, 583, A126
Siebenmorgen, R., Carraro, G., Valenti, E., et al. 2011, Msngr, 144, 9
Skillman, E. D., Hidalgo, S. L., Weisz, D. R., et al. 2014, ApJ, 786, 44
Small, E. E., Bersier, D., & Salaris, M. 2013, MNRAS, 428, 763
Smecker-Hane, T. A., Stetson, P. B., Hesser, J. E., & Vandenberg, D. A. 1996, in ASP Conf. Ser. 98, From Stars to Galaxies: The Impact of Stellar Physics on Galaxy Evolution, ed. C. Leitherer, U. Fritze-von-Alvensleben, & J. Huchra, (San Francisco, CA: ASP), 328
Sohn, S. T., Majewski, S. R., Muñoz, R. R., et al. 2007, ApJ, 663, 960
Stetson, P. B., Monelli, M., Fabrizio, M., et al. 2011, Msngr, 144, 32
Strigari, L. E., Bullock, J. S., Kaplinghat, M., et al. 2008, Natur, 454, 1096
Tolstoy, E., Hill, V., & Tosi, M. 2009, ARA&A, 47, 371
Walker, M. G., Mateo, M., & Olszewski, E. W. 2008, ApJL, 688, L75
Walker, M. G., Mateo, M., & Olszewski, E. W. 2009a, AJ, 137, 3100
Walker, M. G., Mateo, M., Olszewski, E. W., et al. 2007, ApJL, 667, L53
Walker, M. G., Mateo, M., Olszewski, E. W., et al. 2009b, ApJ, 704, 1274
Walker, M. G., & Peñarrubia, J. 2011, ApJ, 742, 20
Woo, J., Courteau, S., & Dekel, A. 2008, MNRAS, 390, 1453